Journal of Computational Physics 229 (2010) 7545–7570

Contents lists available at ScienceDirect

Journal of Computational Physics

journal homepage: www.elsevier.com/locate/jcp

Compact fourth-order finite volume method for numerical solutions of Navier–Stokes equations on staggered grids

Arpiruk Hokpunna, Michael Manhart *

Fachgebiet Hydromechanik, Technische Universität München, Arcisstr. 21, Munich 80333, Germany

ARTICLE INFO

Article history:
Received 17 September 2009
Received in revised form 16 April 2010
Accepted 30 May 2010
Available online 13 June 2010

Keywords:
Finite volume methods
Navier–Stokes equations
Higher-order schemes
Compact schemes
Staggered grids

ABSTRACT

The development of a compact fourth-order finite volume method for solutions of the Navier–Stokes equations on staggered grids is presented. A special attention is given to the conservation laws on momentum control volumes. A higher-order divergence-free interpolation for convective velocities is developed which ensures a perfect conservation of mass and momentum on momentum control volumes. Three forms of the nonlinear correction for staggered grids are proposed and studied. The accuracy of each approximation is assessed comparatively in Fourier space. The importance of higher-order approximations of pressure is discussed and numerically demonstrated. Fourth-order accuracy of the complete scheme is illustrated by the doubly-periodic shear layer and the instability of plane-channel flow. The efficiency of the scheme is demonstrated by a grid dependency study of turbulent channel flows by means of direct numerical simulations. The proposed scheme is highly accurate and efficient. At the same level of accuracy, the fourth-order scheme can be ten times faster than the second-order counterpart. This gain in efficiency can be spent on a higher resolution for more accurate solutions at a lower cost.

© 2010 Elsevier Inc. All rights reserved.

1. Introduction

Over a half century, Computational Fluid Dynamics (CFD) plays an important part helping engineers and scientists to understand the nature of turbulent flows. An accurate time-dependent numerical simulation of turbulent flow can be obtained by direct numerical simulation (DNS) which solve the discrete Navier–Stokes equations directly. DNS can be very accurate but extremely expensive. The complexity of a DNS is roughly rising with $O(Re^{9/4})$. This scaling restricts DNS to low or moderate Reynolds numbers. A promising alternative simulation to DNS is the large eddy simulation (LES) in which the large-scale structures of the flow are resolved and the small-scale structures are modelled.

In an essence of numerical simulations, these two approaches rely heavily on the accuracy of the spatial information of the flow field. A satisfactory simulation cannot be obtained if the dynamics of the flow are not described in a sufficiently accurate way. Modelling effects of the small scales in an LES will not improve the overall accuracy of the solution when the numerical error was larger than the effects of the small scales [1]. The accuracy of the flow field information can be improved by increasing the numerical grid points or increasing the accuracy order of the numerical approximations. The latter approach has become an active field of research in recent years.

Higher-order approximations can be computed explicitly using Lagrange polynomials. The nth order approximation of the mth order derivative requires $n + m$ abscissas. Alternatively, one can couple unknown values to the abscissas and solve a system of linear equations. These implicit approximations have shorter stencils and have been called *compact scheme* by Lele [2]

* Corresponding author. Fax: +49 8928928332.
E-mail addresses: a.hokpunna@bv.tum.de (A. Hokpunna), m.manhart@bv.tum.de (M. Manhart).

0021-9991/$ - see front matter © 2010 Elsevier Inc. All rights reserved.
doi:10.1016/j.jcp.2010.05.042

who demonstrates the superiority of compact schemes over traditional explicit schemes. At intermediate wave numbers, the compact fourth-order scheme is even better than the explicit sixth-order scheme. He quantified the resolution characteristics of second and higher-order schemes and showed that for a relative error of 0.1%, the fourth-order compact differentiation requires 5 points per half-wave, the fourth-order explicit requires 8 grid points and the second-order requires 50. In three-dimensional simulations, the total number of grid points grows cubically while the cost of higher-order schemes is linearly proportional to the second-order scheme. Thus using higher-order schemes is more attractive than a brute force increasing of resolution.

The finite volume methods (FVM) hold a strong position in CFD community because of their intrinsic conservation properties. Despite the popularity of the second-order FVM, there are only a few papers addressing its developments towards higher-order. The complicated relationship of volume-averaged values and surface fluxes made higher-order FVM more difficult than the finite difference (FD) counterpart. The first work that tries to link compact schemes to FVM is presented by Gaitonde and Shang [3]. They present fourth- and sixth-order compact finite volume methods for linear wave phenomena. However, the so-called reconstruction procedure is needed to compute the primitive value, which costs significant computational time. A more economical approach is proposed by Kobayashi [4]. He directly calculates the surface-averaged values from the volume-averaged ones. Explicit and implicit approximations based on the cell-averaged value up to 12th-order are analysed. Pereira et al. [5] present a compact finite volume method for the two-dimensional Navier–Stokes equations on collocated grids. Piller and Stalio [6] propose a compact finite volume method on staggered grids in two dimensions. Lacor et al. [7] develops a finite volume method on arbitrary collocated structured grids and performs LES of a turbulent channel flow at $Re_\tau = 180$. LES of the same flow with explicit filtering is performed in [8] using the spatial discretisation of [5]. Fourth-order finite volume in cylindrical domain is developed in [9] and a DNS of pipe flow at $Re_\tau = 360$ is performed.

Staggered grids have become a favourable arrangement over collocated grids because of the pressure decoupling problem. The pressure decoupling is not confined only in the second-order scheme. This problem is already reported in [5] when using even number of cells with a fourth-order scheme. Recently, a staggered grid has been shown to be more robust than collocated one by Nagarajan et al. [10] in large-eddy simulations. Thus compact finite volume methods on staggered grids deserves more attention.

On staggered grids, there are three problems to solve in order to achieve higher-order accuracy under finite volume discretisation, namely (i) *the approximation of convective velocities*, (ii) *the treatment of nonlinear terms* and (iii) *the discretisation of the pressure term*. The convective process requires the convective velocities on the surfaces of the momentum cells which are defined staggered to the pressure cells. On collocated grids, the face-averaged values of the momentum can be used to approximate the convective velocities because they are positioned correctly. However, on staggered grids the face-averaged momentums are aligned differently and the convective velocities must be interpolated accordingly. A simple interpolation, however, can violate the conservation of mass on the momentum cells. Higher-order divergence-free interpolations are still an open issue. The treatment of nonlinearity of the convective fluxes over the cell surface was addressed by Pereira et al. [5]. Nevertheless, the reconstruction of the nonlinear fluxes must be chosen wisely. The role of the pressure term in higher-order methods is still a matter of controversy among researchers in this field. It has been shown in [11–13] that the approximation of the pressure term has to be the same order as the one of the convective and diffusive fluxes. When the pressure is approximated using lower order, the overall accuracy is limited by this approximation. In [6,14] the second-order solution of pressure is found to be sufficient for a fourth-order accurate solution of velocities. This issue must be clarified because it is crucial to the cost of computations. The solution of the pressure can easily take more than half of the computation time. If a second-order approximation of the Poisson equation for the pressure was sufficient, then the higher-order accuracy of the momentum can be achieved at a marginal cost. However, if a fourth-order treatment of the pressure is necessary, a 19-point stencil of the Laplacian operator must be used instead of a simple 7-point stencil.

In the present work, we have two objectives. The first objective is to present the development of a fourth-order method for finite volume discretisation of the Navier–Stokes Equations by solving the questions posed in the previous paragraph. We propose a novel interpolation that preserves the discrete divergence-free property of the velocity fields. This method is generalized for arbitrary order of accuracy. Another fourth-order convective velocity that is not divergence-free is presented for comparison. Several choices of nonlinear corrections and the role of the pressure term are studied. We present new cell-centered deconvolutions for the mass and pressure fluxes. These approximations are explicit and lead to a banded system of the Poisson equation given by the projection method. The higher resolution properties of these cell-centered deconvolutions are demonstrated by the comparative Fourier analysis. We show that the solution of the pressure with lower order indeed limits the accuracy of the solution. However, this limitation on staggered grids is not as severe as on collocated ones reported in [11]. We use Fourier analysis to show that staggered grids can satisfy the incompressibility constraint in a better way than collocated grids and more information can be retained in the flow field.

The second objective of this work is to verify whether the fourth-order scheme can out perform the second-order scheme in terms of accuracy and efficiency. Despite the fact that higher-order schemes are shown to be vastly superior to second-order schemes in laminar flows by numerous authors, some recent papers report disappointing findings in the application of higher-order schemes to turbulent flows. Gullbrand [15] applies the fully-conservative explicit fourth-order scheme of Morinishi et al. [16] and Vasilyev [17] to a DNS of turbulent channel flow. Knikker [13] developed a compact finite difference method and applied it to the same flow. The grid resolutions used in their simulations are comparable to those used by the spectral code in [18]. They both report that differences between the results from second-order and fourth-order schemes are negligible and these results are significantly different from the spectral code. Meinke et al. [19] comment that the sixth-order

compact scheme is comparable to the second-order upwind scheme in large-eddy simulation of turbulent channel and jet flows. Shishkina and Wagner [9] also note a similar finding in their DNS of turbulent pipe flow but pointed out that the fourth-order scheme improves the third- and the fourth-order statistics. In this work we will show that in a turbulent channel flow, our fourth-order scheme can deliver a comparable result to the second-order scheme using only one-eight number of cells used by the second-order scheme.

Standard test cases with increasing complexity are used to validate the proposed scheme. First we evaluate the accuracy of each approximation in the Navier–Stokes equations and identify the determinant of the accuracy by approximating a Gaussian function. Next, the fourth-order convergence of the full discretisation of the Navier–Stokes equations is demonstrated in a doubly periodic shear layer flow. The proposed schemes including the boundary closures are examined by monitoring the growth of a perturbation in a plane-channel flow. The quality and the efficiency of the proposed scheme is finally evaluated using direct numerical simulations of turbulent channel flows at $Re_\tau = 180$ and 590.

2. Navier–Stokes equations and staggered grid system

In this section, we introduce the governing equations for incompressible flows we intend to solve using a finite volume method. A staggered grid system is defined and the discrete forms of the Navier–Stokes equations (NSE) are discussed.

2.1. Navier–Stokes equation

We solve the Navier–Stokes equations for incompressible flows of a Newtonian fluid in absence of external forces. The integral forms of the conservation laws of mass and momentum used for finite volume methods read as

$$\oint_A \mathbf{u}\cdot\mathbf{n}\,dA = 0, \tag{1}$$

$$\frac{\partial}{\partial t}\int_\Omega \mathbf{u}\,d\Omega + \oint_A (\mathbf{uu})\cdot\mathbf{n}\,dA = \nu\oint_A \mathbf{T}\,dA - \frac{1}{\rho}\oint_A p\cdot\mathbf{n}\,dA. \tag{2}$$

Here, $\mathbf{u}$ defines the velocity vector, p the pressure, $\mathbf{T}$ the strain rate tensor, ρ the density and ν the kinematic viscosity of the fluid while $\mathbf{n}$ is the unit vector on dA pointing outside of the volume Ω.

2.2. Staggered grid system

On Cartesian grids, a system of staggered grids (Fig. 1) can be set up by putting collocated grid points along a real line x using a strictly increasing function $\xi(i)$, $x_i = \xi(i)$, $i = 0,\ldots,nx+1$. Staggered grid points are defined by $xs_i = \frac{1}{2}(x_i + x_{i+1})$, $i = 0,\ldots,nx$. The control volume ΩS_i of the momentum u_{is} is defined on the closed interval $[x_i, x_{i+1}]$, likewise the control volume of the pressure cells is defined by $\Omega_i = [xs_{i-1}, xs_i]$. In this setting, half indices mark the position of the control surface of the corresponding control volumes (full indices) e.g. $xs_{i+1/2}$ is the x position of the East face of ΩS_i which is corresponding to x_{i+1}. This leads to the following mapping between two indices, $xs_{i+1/2} = x_{i+1}$ and $x_{i+1/2} = xs_i$. We explicitly call the vector of staggered grid point as xs to emphasize that $xs_i = \frac{1}{2}(\xi(i) + \xi(i+1)) \neq \xi(i+\frac{1}{2})$. This setting allows an accurate calculation of divergence on the pressure cell because surfaces of pressure cells are placed exactly at the middle of the momentum cells.

The finite volume method describes the changes of a volume-averaged quantity by the net fluxes on the surface enclosing that control volume. These fluxes are surface-averaged quantity. In a second-order context, pointwise, surface-averaged and cell-averaged values are interchangeable because the second-order local truncation error is acceptable. In higher-order

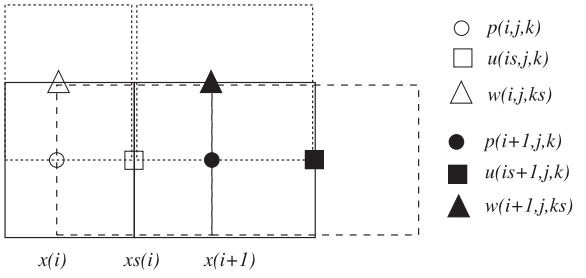

Fig. 1. Arrangement of variables on a non-uniform staggered grids consisting of pressure cells (solid), u-momentum (dash) and w-momentum (dotted) cells.

context, they are not and must be well identified. In this paper, a cell-averaged value of f defined on a collocated control volume $\Omega_{i,j,k} = \Delta x_i \Delta y_j \Delta z_k$ is denoted by

$$[f]^{xyz}_{i,j,k} = \frac{1}{\Omega_{i,j,k}} \int_{x_{i-1/2}}^{x_{i+1/2}} \int_{y_{j-1/2}}^{y_{j+1/2}} \int_{z_{k-1/2}}^{z_{k+1/2}} f(x,y,z)\, dx\, dy\, dz. \tag{3}$$

Accordingly, the cell-averaged value of an x-staggered variable g on $\Omega S_{is,j,k} = \Delta xs_i \Delta y_j \Delta z_k$ is represented by

$$[g]^{xyz}_{is,j,k} = \frac{1}{\Omega S_{is,j,k}} \int_{xs_{i-1/2}}^{xs_{i+1/2}} \int_{y_{j-1/2}}^{y_{j+1/2}} \int_{z_{k-1/2}}^{z_{k+1/2}} g(x,y,z)\, dx\, dy\, dz. \tag{4}$$

In order to make a distinction of averaged values defined on staggered grid points from the collocated ones, the s is appended to the indices. Here is stands for the ith staggered grid point, $x = xs(i)$. For example $[u]^{xyz}_{is,j,k}$ is half-a-cell staggered from $[p]^{xyz}_{i,j,k}$ in the positive x-direction. Surface and line-averaged values can be defined in a similar way by reducing the dimension of integration to two and one respectively. For example $[p]^{yz}_{is,j,k}$ is surfaced-averaged value of p on the yz-plane located at xs_i.

2.3. Discrete form of Navier–Stokes equations

In this section, we introduce the finite volume discretisation of the Navier–Stokes equations and explain the necessity of the mass conservation on the momentum cells.

2.3.1. Conservation of mass

In incompressible flows, the conservation of the mass flux is equivalent to the conservation of the volume flux and they will be used interchangeably. On staggered grids, it is convenient to enforce the mass conservation on the control volumes of the pressure (Ω_i) where the divergence $[div]^{xyz}_{i,j,k}$ from these cells is given by

$$[div]^{xyz}_{i,j,k} \Delta x_i \Delta y_j \Delta z_k = \left([u]^{yz}_{i+\frac{1}{2},j,k} - [u]^{yz}_{i-\frac{1}{2},j,k}\right)\Delta y_j \Delta z_k + \left([v]^{xz}_{i,j+\frac{1}{2},k} - [v]^{xz}_{i,j-\frac{1}{2},k}\right)\Delta x_i \Delta z_k + \left([w]^{xy}_{i,j,k+\frac{1}{2}} - [w]^{xy}_{i,j,k-\frac{1}{2}}\right)\Delta x_i \Delta y_j. \tag{5}$$

The mass conservation dictates that this divergence is zero.

2.3.2. Conservation of momentum

Eq. (2) describes the conservation of the momentum per unit mass. On a staggered grid, we conserve the three components: $[u]^{xyz}_{is,j,k}$, $[v]^{xyz}_{i,js,k}$ and $[w]^{xyz}_{i,j,ks}$ for the momentum in x, y and z, respectively. Let us consider the discrete form of the momentum equation for the first component:

$$\Omega S_{is,j,k} \frac{\partial [u]^{xyz}_{is,j,k}}{\partial t} = -\mathscr{C}_{is,j,k} + \nu \mathscr{D}_{is,j,k} - \frac{1}{\rho} \mathscr{P}_{is,j,k}. \tag{6}$$

The terms $\mathscr{C}_{is,j,k}, \mathscr{D}_{is,j,k}$ and $P_{is,j,k}$ are shorthand notations of net convective, diffusive and pressure fluxes, respectively. On a Cartesian grid they are defined as follows:

$$\mathcal{C}_{is,j,k} = \left([\mathsf{u}u]^{yz}_{is+\frac{1}{2},j,k} - [\mathsf{u}u]^{yz}_{is-\frac{1}{2},j,k}\right)\Delta y_j \Delta z_k + \left([\mathsf{v}u]^{xz}_{is,j+\frac{1}{2},k} - [\mathsf{v}u]^{xz}_{is,j-\frac{1}{2},k}\right)\Delta xs_{is} \Delta z_k + \left([\mathsf{w}u]^{xy}_{is,j,k+\frac{1}{2}} - [\mathsf{w}u]^{xy}_{is,j,k-\frac{1}{2}}\right)\Delta xs_{is} \Delta y_j. \tag{7}$$

$$\mathcal{D}_{is,j,k} = \left(\left[\frac{\partial u}{\partial x}\right]^{yz}_{is+\frac{1}{2},j,k} - \left[\frac{\partial u}{\partial x}\right]^{yz}_{is-\frac{1}{2},j,k}\right)\Delta y_j \Delta z_k + \left(\left[\frac{\partial u}{\partial y}\right]^{xz}_{is,j+\frac{1}{2},k} - \left[\frac{\partial u}{\partial y}\right]^{xz}_{is,j-\frac{1}{2},k}\right)\Delta xs_{is} \Delta z_k + \left(\left[\frac{\partial u}{\partial z}\right]^{xy}_{is,j,k+\frac{1}{2}} - \left[\frac{\partial u}{\partial z}\right]^{xy}_{is,j,k-\frac{1}{2}}\right)\Delta xs_{is} \Delta y_j. \tag{8}$$

$$\mathcal{P}_{is,j,k} = \left([p]^{yz}_{is+\frac{1}{2},j,k} - [p]^{yz}_{is-\frac{1}{2},j,k}\right)\Delta y_j \Delta z_k + \left([p]^{xz}_{is,j+\frac{1}{2},k} - [p]^{xz}_{is,j-\frac{1}{2},k}\right)\Delta xs_{is} \Delta z_k + \left([p]^{xy}_{is,j,k+\frac{1}{2}} - [p]^{xy}_{is,j,k-\frac{1}{2}}\right)\Delta xs_{is} \Delta y_j. \tag{9}$$

Here we introduce a distinction of the two velocities in the convective term into convective velocities and the convected velocities. The convective velocities are denoted by Sans-serif fonts u, v and w. The convected velocities (momentum per unit mass) are denoted by italic font u, v and w. It is important to note that the convective velocities have to be conservative, i.e. the divergence over the momentum cells has to be zero. If the convective velocities were not mass-conservative, an additional source term,

$$[s]^{xyz}_{is,j,k} \approx [div]^{xyz}_{is,j,k} [u]^{xyz}_{is,j,k} \tag{10}$$

will be added to the r.h.s. of momentum equation (Eq. (6)). Although this source term does not affect the global conservation of the momentum due to the telescoping property of FVM, the quality of the local solution is degraded and the Galilean invariant is violated as well.

All the discrete equations in this section are exact and no simplifications or approximations have been introduced so far. Approximation errors will be introduced when these fluxes are approximated from the volume-averaged values.

3. Numerical approximations

In this section, we describe, for each term in the discrete Navier–Stokes equations, how it can be approximated by a fourth-order method. First the approximation for mass flux is presented, followed by the cell-centered approximation for the pressure. Then approximations of convective and diffusive fluxes for the momentum using the compact fourth-order approximations of Kobayashi [4] are briefly described. A novel approximation of divergence-free convective velocities is presented. Finally the nonlinear corrections for staggered grids are discussed.

3.1. Cell-centered deconvolution for the computation of mass fluxes

The enforcement of the mass conservation in Eq. (5) requires the approximation of the surface-averaged values at the center of the momentum cells from the volume-averaged ones, which is called deconvolution. The second-order cell-centered deconvolution (the mid-point rule) can be improved to fourth-order by using this explicit formula:

$$[u]^{yz}_{is,j,k} = \beta_1 [u]^{xyz}_{is-1,j,k} + \beta_2 [u]^{xyz}_{is,j,k} + \beta_3 [u]^{xyz}_{is+1,j,k}. \tag{11}$$

The coefficients of this deconvolution can be found by Taylor expansion or the method of undetermined coefficients. On uniform grids they are $\beta_1 = \beta_3 = -\frac{1}{24}$ and $\beta_2 = \frac{13}{12}$. Let $h_{is-1} = \Delta x s_{is-1}$, $h_{is} = \Delta x s_{is}$ and $h_{is+1} = \Delta x s_{is+1}$ the coefficients on non-uniform grids are given by the following formulas:

$$\beta_1 = -\frac{h_{is}^2}{4(h_{is-1}+h_{is})(h_{is-1}+h_{is}+h_{is+1})}, \quad \beta_2 = 1-(\beta_1+\beta_3), \quad \beta_3 = -\frac{h_{is}^2}{4(h_{is}+h_{is+1})(h_{is-1}+h_{is}+h_{is+1})}.$$

Here we do not explicitly compute β_2 from the grid spacing, but the consistency criterion is used instead. We call this approximation *cell-centered deconvolution* because it approximates the surface-averaged values at the center of the cells from the volume-averaged ones.

3.2. Cell-centered deconvolution for the pressure

The fourth-order deconvolution of the pressure on the surface of the momentum cells reads

$$[p]^{yz}_{i,j,k} = \beta_4 [p]^{xyz}_{i-1,j,k} + \beta_5 [p]^{xyz}_{i,j,k} + \beta_6 [p]^{xyz}_{i+1,j,k}. \tag{12}$$

Note that, even if the stencil is exactly the same as in the previously introduced cell-centered deconvolution, the coefficients can be different when the grid is not uniform. This is because the deconvolved values are not lying on the center of the cells and the following coefficients must be used:

$$\beta_4 = \frac{2h_{is}^2 + h_{is}h_{is+1} - h_{is-1}3h_{is} - h_{is-1}h_{is+1}}{(h_{is}+2h_{is-1}+h_{is-2})K_1}, \quad \beta_5 = 1-(\beta_4+\beta_6), \quad \beta_6 = -\frac{2h_{is-1}^2 + h_{is-1}h_{is-2} - h_{is-1}3h_{is} - h_{is}h_{is-2}}{(h_{is-1}+2h_{is}+h_{is+1})K_1},$$

$$K_1 = h_{is-2} + 2h_{is-1} + 2h_{is} + h_{is+1}.$$

This cell-centered deconvolution is fourth-order on uniform grids and third-order on non-uniform grids. Nonetheless, it is more accurate than other approximations presented here, as will be demonstrated later in Section 6.

3.3. Intercell deconvolution for the computation of momentum fluxes

According to Eq. (7), the convected velocities u on the surface enclosing the staggered control volumes are needed. In contrast to Eq. (11) where the deconvoluted quantity is located at *the center of the volume-averaged one*, here the desired surface-averaged fluxes are needed at the *interfaces between momentum cells* i.e. between the volume-averaged quantities. We call this an *intercell-deconvolution*. These surface-averages of the momentum are positioned at nonstaggered grid points e.g. x_i and they can be approximated by the following fourth-order compact deconvolution [4]:

$$\alpha_1 [u]^{yz}_{i-1,j,k} + [u]^{yz}_{i,j,k} + \alpha_2 [u]^{yz}_{i+1,j,k} = \beta_7 [u]^{xyz}_{is-1,j,k} + \beta_8 [u]^{xyz}_{is,j,k}. \tag{13}$$

The stencil of this approximation is depicted in Fig. 2. Note that $[u]^{yz}_{i,j,k}$ here is equivalent to $[u]^{yz}_{is-\frac{1}{2},j,k}$ in Eq. (7). On uniform grids, $\alpha_1 = \alpha_2 = \frac{1}{4}$ and $\beta_7 = \beta_8 = \frac{3}{4}$. The coefficients on non-uniform grids are:

$$\alpha_1 = \frac{h_{is}^2}{(h_{is}+h_{is-1})^2}, \quad \alpha_2 = \frac{h_{is-1}^2}{(h_{is}+h_{is-1})^2}, \quad \beta_7 = \frac{2h_{is}^2(h_{is}+2h_{is-1})}{(h_{is}+h_{is-1})^3}, \quad \beta_8 = \frac{2h_{is}^2(h_{is-1}+2h_{is})}{(h_{is}+h_{is-1})^3}.$$

It is possible to tune these coefficients in the Fourier space and obtain a better resolution for high wave numbers [2,20], however, at the expense of the asymptotic convergence rate. In this paper, we aim to construct a genuine fourth-order numerical scheme for the Navier–Stokes equations, therefore only formal fourth-order schemes are studied here.

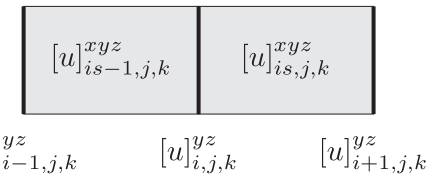

Fig. 2. The stencil of compact fourth-order intercell deconvolution in Eq. (13).

3.4. Intercell differentiation for diffusive fluxes

The compact fourth-order approximation of the first derivative, for example $[\partial u/\partial z]^{yz}_{is+1/2,j,k}$ in Eq. (8), is approximated based on the same stencil used earlier in Eq. (13) and the differentiation formula is given by

$$\alpha_3\left[\frac{\partial u}{\partial x}\right]^{yz}_{i-1,j,k}+\left[\frac{\partial u}{\partial x}\right]^{yz}_{i,j,k}+\alpha_4\left[\frac{\partial u}{\partial x}\right]^{yz}_{i+1,j,k}=\beta_9[u]^{xyz}_{is-1,j,k}+\beta_{10}[u]^{xyz}_{is,j,k}. \tag{14}$$

The coefficients on non-uniform grids are

$$\alpha_3=\frac{h_{is}(h^2_{is-1}+h_{is-1}h_{is}-h^2_{is})}{K},\quad \alpha_4=\frac{(h^2_{is}+h_{is-1}h_{is}-h^2_{is-1})h_{is-1}}{K},\quad \beta_9=\frac{-12h_{is-1}h_{is}}{K},\quad \beta_{10}=\frac{12h_{is-1}h_{is}}{K},$$

$$K=(h_{is}+h_{is-1})\left(h^2_{is}+3h_{is-1}h_{is}+h^2_{is-1}\right).$$

The fourth-order intercell deconvolution given previously is fourth-order accurate as well on non-uniform grids but the compact differentiation here is third-order on non-uniform grids. However, the transfer function of Eq. (14) is superior to the one of Eq. (13) and therefore the fourth-order convergence is not compromised as will be shown later.

3.5. Convective velocities

The convective fluxes in Eq. (7) consist of the product of convective velocity (u, v and w) with the convected velocity u, v and w. Naturally without being concerned about the mass conservation over momentum cells, one could use the deconvoluted momentum (per unit mass) $[u]^{yz}_{i,j,k}$, in Eq. (13) as the convective velocity $[\mathrm{u}]^{yz}_{i,j,k}$. The approximation of the remaining convective velocities e.g. $[\mathrm{v}]^{xz}_{is,js,k}$ and $[\mathrm{w}]^{xy}_{is,j,ks}$ can be done in various ways using the known cell-averaged and face-averaged velocities. Piller and Stalio [6] propose to use compact interpolations by first approximating the velocities on the surfaces of the pressure cell e.g. $[\mathrm{w}]^{xy}_{i,j,ks}$ and then apply another compact interpolation to shift these velocities to the faces of momentum cells e.g. $[\mathrm{w}]^{xy}_{is,j,ks}$ where they can be used to convect the momentum fluxes. Here we present a more compact form of a fourth-order interpolation. This interpolation only utilizes the information on the two cells enclosing the interested surface (see Fig. 3). The compact interpolation for the convective velocity $[\mathrm{w}]^{xy}_{is,j,ks}$ reads

$$[\mathrm{w}]^{xy}_{is,j,ks}=k_1-k_2-k_3+R(\Delta^4), \tag{15}$$

where,

$$k_1=\frac{6}{8}\left([w]^{xyz}_{is-\frac{1}{2},j,ks}+[w]^{xyz}_{is+\frac{1}{2},j,ks}\right),$$
$$k_2=\frac{1}{8}\left([w]^{yz}_{is+1,j,k}-2[w]^{yz}_{is,j,k}+[w]^{yz}_{is-1,j,k}\right),$$
$$k_3=\frac{1}{8}\left([w]^{xy}_{is-\frac{1}{2},j,ks-\frac{1}{2}}+[w]^{xy}_{is+\frac{1}{2},j,ks-\frac{1}{2}}+[w]^{xy}_{is+\frac{1}{2},j,ks+\frac{1}{2}}+[w]^{xy}_{is-\frac{1}{2},j,ks+\frac{1}{2}}\right).$$

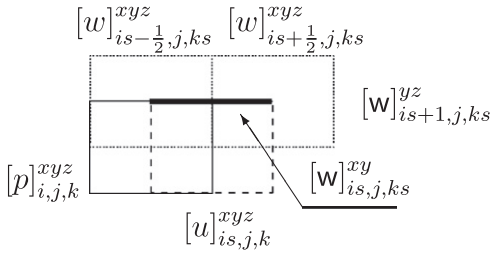

Fig. 3. Approximation stencil of $[\mathrm{w}]^{xy}_{is,j,k+\frac{1}{2}}$ in Eq. (15). The solid box is the pressure cell, the dashed box is the u-momentum cell and dotted boxes are the w-momentum cells.

The leading remainder terms are

$$R = -\frac{1}{384}\frac{\partial^4 w}{\partial x^4}\Delta x^4 - \frac{1}{192}\frac{\partial^4 w}{\partial x^2 z^2}\Delta x^2 \Delta z^2 - \frac{1}{1920}\frac{\partial^4 w}{\partial z^4}\Delta z^4.$$

This stencil is as small as the second-order stencil thus it does not require extra boundary closures. The surface-averaged velocities obtained from the two interpolations in Eqs. (13) and (15) can be used as convective velocities. These convective velocities are fourth-order accurate but not necessarily mass-conservative. We denote these convective velocities as *T*4.

3.6. Divergence-free convective velocities

The divergence-free property of the convective velocities has been addressed by Verstappen and Veldman [21]. They show that it is a necessary condition for the energy conservation. In their work, the fourth-order solution of the convective terms is not computed from a direct fourth-order approximation, but rather a Richardson extrapolation from second-order solutions of a small control volume and a larger one. A direct computation of fourth-order convective velocities is thus avoided. This approach ensures the mass and energy conservation on momentum cells but it is using a stencil width of 7-*h* in each direction for one momentum cell. This wide stencil can reduce the resolution properties of the scheme. In this section we propose a new divergence-free interpolation which only requires a stencil width of 4-*h*.

3.6.1. Concept

The simplest way of computing divergence-free convective velocities is to use a linear combination of the volume fluxes that are already divergence-free. This means we should compute the convective velocities from the volume fluxes over the surface of the pressure cells in which the continuity is enforced. For example, the convective velocity of the *u*-momentum can be computed from the volume fluxes on neighbouring pressure cells sharing the same *x*-coordinate. The remaining difficulty is that we have to work with two directions of fluxes. In the first, the fluxes are aligned with the momentum e.g. the approximation of u for *u*-momentum. In the second, the fluxes are normal to the momentum e.g. the approximation of w for *u*-momentum. These fluxes are defined on different positions and when the grid was not uniform, they would require a different set of coefficients.

Now, we consider the discrete divergence written as a summation of matrix–vector multiplications:

$$D_x u + D_y v + D_z w = div. \tag{16}$$

Any linear transformations matrix *T* applied to this equation will not change the summation. This means if the same interpolation was used for all three velocities, the mass conservation will remain unchanged. Using constant coefficient is of course one of the possibilities, but this does not give a fourth-order convergence. In order to use the same interpolation, we have to convert one of the fluxes into a compatible form with the other one.

The interpolation of the fluxes aligned with the momentum can be done easily using Lagrange interpolations. Therefore we choose to convert the fluxes normal to the direction of the momentum. Inspired by the primitive value reconstruction of Gaitonde and Shang [3], we convert the fluxes normal to the direction of the momentum to line averaged ones such that the same interpolation can be used. To this end, we invoke the second fundamental theorem of Calculus:

$$\int_a^b f(x) = F(b) - F(a), \tag{17}$$

$$F = \int f(x). \tag{18}$$

In two dimensions, the surface-averaged value of the volume flux on the top of pressure cell and the associated line-averaged primitive are related by

$$[w]^{xy}_{i,j,ks} = \frac{1}{\Delta x_i}\left([W]^{y}_{is,j,ks} - [W]^{y}_{is-1,j,ks}\right). \tag{19}$$

The primitive values can be reconstructed at the top of the East and West faces of the pressure cell using this formula. We can now interpolate these values using the same method as was used for u. After that, the interpolated primitive values can be converted back to surface-averaged values using the same relationship. These two conversions are exact. However, a direct implementation of the above method is expensive. A total floating point operations of $8m$ is required for the $(2m)$th-order interpolation, instead of just $4m - 1$. The novelty of our approach is the elimination of these extra costs.

In what follows, we derive a method to approximate the second-order divergence-free convective velocities and generalize the method for arbitrary order of accuracy.

3.6.2. Second-order divergence-free convective velocities

To derive an expression for the convective velocities which is divergence-free and second-order accurate, we start from the mass conservation equation of the *u*-momentum cell on $\Omega S_{i,j,k}$:

$$[div]^{xyz}_{is,j,k}\Delta xs_i\Delta y_j\Delta z_k = \left([\mathrm{u}]^{yz}_{i+1,j,k} - [\mathrm{u}]^{yz}_{i,j,k}\right)\Delta y_j\Delta z_k + \left([\mathrm{v}]^{xz}_{is,js,k} - [\mathrm{v}]^{xz}_{is,js-1,k}\right)\Delta xs_i\Delta z_k + \left([\mathrm{w}]^{xy}_{is,j,ks} - [\mathrm{w}]^{xy}_{is,j,ks-1}\right)\Delta xs_i\Delta y_j. \tag{20}$$

Applying the second fundamental theorem of Calculus to the above equation leads to

$$[div]^{xyz}_{is,j,k}\Delta xs_i\Delta y_j\Delta z_k = \left([\mathrm{u}]^{yz}_{i+1,j,k} - [\mathrm{u}]^{yz}_{i,j,k}\right)\Delta y_j\Delta z_k + \left[\left([\mathrm{V}]^{z}_{i+1,js,k} - [\mathrm{V}]^{z}_{i,js,k}\right) - \left([\mathrm{V}]^{z}_{i+1,js-1,k} - [\mathrm{V}]^{z}_{i,js-1,k}\right)\right]\Delta z_k + \left[\left([\mathrm{W}]^{y}_{i+1,j,ks} - [\mathrm{W}]^{y}_{i,j,ks}\right) - \left([\mathrm{W}]^{y}_{i+1,j,ks-1} - [\mathrm{W}]^{y}_{i,j,ks-1}\right)\right]\Delta y_j. \tag{21}$$

The divergence of the convective velocities is expressed in terms of variables given at x_i and x_{i+1}. A desired variable f at x_i can be obtained by a second-order interpolation using the respective variables from xs_{i-1} and xs_i by the following formula:

$$f_i = \gamma_{i,1}f_{is-1} + \gamma_{i,2}f_{is}, \tag{22}$$

where $\gamma_{i,1}$ and $\gamma_{i,2}$ are the respective interpolation coefficients. The reconstruction of the primitive values of w on the pressure cells can be started by assuming that $[\mathrm{W}]^{y}_{is-1,j,k}$ is known and the subsequent primitive values can be computed using Eq. (19) together with Eq. (22). Together with Eqs. (19) and (22) we obtain

$$[\mathrm{w}]^{xy}_{is,j,ks}\Delta x_{is} = \gamma_{i+1,1}[\mathrm{W}]^{y}_{is,j,ks} + \gamma_{i+1,2}[\mathrm{W}]^{y}_{is+1,j,ks} - \gamma_{i,1}[\mathrm{W}]^{y}_{is-1,j,ks} - \gamma_{i,2}[\mathrm{W}]^{y}_{is,j,ks}. \tag{23}$$

After regrouping of variables, the convective velocity on the top surface of $[u]^{xyz}_{is,j,k}$ is given by

$$[\mathrm{w}]^{xy}_{is,j,ks} = \theta_0[\mathrm{W}]^{y}_{is-1,j,ks} + \theta_1[w]^{xy}_{i,j,ks} + \theta_2[w]^{xy}_{i+1,j,ks} \tag{24}$$

with,

$$\theta_0 = \frac{1}{\Delta x_{is}}(\gamma_{i+1,1} + \gamma_{i+1,2}) - (\gamma_{i,1} + \gamma_{i,2})),$$
$$\theta_1 = \frac{\Delta x_i}{\Delta x_{is}}((\gamma_{i+1,1} + \gamma_{i+1,2}) - \gamma_{i,2}),$$
$$\theta_2 = \frac{\gamma_{i+1,2}\Delta x_{i+1}}{\Delta x_{is}}.$$

The coefficient of the unknown primitive value, $[\mathrm{W}]^{y}_{is-1,j,k}$ is reduced to a difference between the sum of two sets of interpolation coefficients. The consistency dictates that the sum of any set of interpolation coefficients is equal to unity thus $\theta_0 = 0$ and $[\mathrm{W}]^{y}_{is-1,j,k}$ can be removed from the interpolation. This leads to a convenient way of computing convective velocities using the new set of interpolation coefficients, θ. In this formulation, the construction of primitive values and the back transformation are fully avoided.

The net volume flux leaving the control volume of $\Omega_{is,j,k}$ under the second-order divergence-free interpolation is

$$[div]^{xyz}_{is,j,k} = \gamma_{i,1}[div]^{xyz}_{i,j,k} + \gamma_{i+1,2}[div]^{xyz}_{i+1,j,k}. \tag{25}$$

This equation indicates that the imbalance of mass fluxes at the momentum cell is of the same order of magnitude as the one enforced at the pressure cells.

3.6.3. Fourth-order divergence-free convective velocities

A fourth-order Lagrange interpolation formula for the convective velocity $[\mathrm{u}]^{yz}_{i,j,k}$ at the cell face in x-direction of the u momentum can be obtained by

$$[\mathrm{u}]^{yz}_{i,j,k} = \gamma_{i,1}[\mathrm{u}]^{yz}_{is-2,j,k} + \gamma_{i,2}[\mathrm{u}]^{yz}_{is-1,j,k} + \gamma_{i,3}[\mathrm{u}]^{yz}_{is,j,k} + \gamma_{i,4}[\mathrm{u}]^{yz}_{is+1,j,k}. \tag{26}$$

The coefficients of this interpolation are the same as the ones for a fourth-order Lagrange interpolation of pointwise values. We can proceed with the similar procedure as in the second-order divergence-free interpolation and arrive at

$$[\mathrm{w}]^{xy}_{is,j,ks} = \theta_{is,1}[\mathrm{w}]^{xy}_{i-1,j,ks} + \theta_{is,2}[\mathrm{w}]^{xy}_{i,j,ks} + \theta_{is,3}[\mathrm{w}]^{xy}_{i+1,j,ks} + \theta_{is,4}[\mathrm{w}]^{xy}_{i+2,j,ks}. \tag{27}$$

We call this convective velocity *DF4*. On uniform grids, the two sets of interpolating coefficients $\gamma_{i,1-4}$ and θ_{1-4} are $\left[\frac{-1}{16}, \frac{9}{16}, \frac{9}{16}, \frac{-1}{16}\right]$, in numerical order. The divergence-free interpolation of the convective velocities can be generalised for arbitrary order. Suppose that a $(2m)$th-order Lagrange interpolation is used instead of Eq. (26), then the $(2m)$th-order divergence-free interpolation of the convective velocity on the top surface of the u-momentum cell is given by

$$[\mathrm{w}]^{xy}_{is,j,ks} = \sum_{l=1}^{2m}\left(\theta_{is,l}[\mathrm{w}]^{xy}_{i-m+l,j,ks}\right) \tag{28}$$

with,

$$\theta_{is,l} = \left(\sum_{j=l}^{2m} \gamma_{i+1\,j} - \sum_{j=l+1}^{2m} \gamma_{i\,j} \right) \frac{\Delta x_{i-m+l}}{\Delta x_{is}}. \tag{29}$$

Identical coefficients are used for v. This higher-order divergence-free interpolation can be applied for any position in the field.

3.7. Nonlinear correction

The convective term $[\mathsf{u}_\mathbf{j} u_\mathbf{i}]$ is the origin of the nonlinearity in the Navier–Stokes equations. This term is responsible for energy transfer between different scales and wave components smaller than the Nyquist limit can be created by it. In finite difference methods the product of u_j and u_i is the exact value of $\mathsf{u}_i u_j$. On the other hand, the approximation of the nonlinear term in finite volume methods using $[\mathsf{u}_\mathbf{j} u_\mathbf{i}] = [\mathsf{u}_\mathbf{i}][u_\mathbf{j}]$ is only second-order accurate. Additional operations are needed to achieve higher-order accuracy in finite volume methods. In this work we use variants of the nonlinear correction approach proposed by Pereira et al. [5].

A fourth-order accurate approximation of a nonlinear term can be obtained by adding some corrections to the second-order approximation:

$$[fg]^{yz} = [f]^{yz}[g]^{yz} + \frac{\Delta y^2}{12}\frac{\partial f}{\partial y}\frac{\partial g}{\partial y} + \frac{\Delta z^2}{12}\frac{\partial f}{\partial z}\frac{\partial g}{\partial z} + O(\Delta y^4, \Delta z^4). \tag{30}$$

The original formula of [5] computes the correction term from the cell-averaged values. First the second-order interpolation is used to compute the face-averaged values then the computed values are used for the approximation of the first-derivative. Here, we use the surface-averaged values which are readily available from the approximation of the momentum fluxes (Eq. (13)). The use of the surface-averaged values allows a cheaper computation and better resolution characteristics. The fourth-order approximation for the convection term on the East face of u-momentum is given by:

$$[\mathsf{uu}]^{yz}_{i+1\,j,k} = [\mathsf{u}]^{yz}_{i+1\,j,k}[u]^{yz}_{i+1\,j,k} + \frac{1}{48}\left([u]^{yz}_{i+1\,j+1,k} - [u]^{yz}_{i+1\,j-1,k}\right)^2 + \frac{1}{48}\left([u]^{yz}_{i+1\,j,k+1} - [u]^{yz}_{i+1\,j,k-1}\right)^2. \tag{31}$$

On the top face we use the following formula:

$$[\mathsf{wu}]^{xy}_{is\,j,ks} = [\mathsf{w}]^{xy}_{is\,j,ks}[u]^{xy}_{is\,j,ks} + \frac{1}{24}\left([u]^{xy}_{is+1\,j,ks} - [u]^{xy}_{is-1\,j,ks}\right)\left([w]^{xyz}_{i+1\,j,ks} - [w]^{xyz}_{i\,j,ks}\right) + \frac{1}{24}\left([u]^{xy}_{is\,j+1,k} - [u]^{xy}_{is\,j-1,k}\right)\left([w]^{xz}_{i\,js,k} - [w]^{xz}_{i\,js-1,k}\right). \tag{32}$$

The proposed forms above are one of many possibilities. In Section 6.2 we consider some other possible forms of nonlinear corrections. However, the proposed forms here are the most accurate.

4. Projection method

When the momentum equation is integrated in time, the new velocity fields are not necessarily divergence-free and thus usually called provisional velocities. One of the most successful approaches ensuring the mass-conservation after the time integration is the fractional time step method (FTSM) which operates on these provisional velocities. Traditionally there are two classes of the FTSM namely *pressure-Poisson* and *projection methods* [22]. The pressure-Poisson method does not truly solve for the pressure itself, instead, it solves for a pressure-like variable ϕ which is a Lagrange multiplier for a divergence-free velocity field that is closest to the provisional velocity field. On the other hand, projection methods solve for the divergence-free field which has the same vorticity as the provisional velocity. Both approaches have to solve a Poisson equation, but with a different form of the discrete Laplacians.

Consider the explicit Euler time integration of u-momentum. Let $\mathbf{u}^n$ be the velocity and $\mathbf{H}^n$ be the contribution from convective and diffusive terms at time t_n. Let $\mathbf{u}^*$ be the provisional velocity evaluated without the pressure term and $\mathbf{u}^{n+1}$ be the divergence-free velocity field at the new time step when a suitable p is used. The equations for $\mathbf{u}^*$ and $\mathbf{u}^{n+1}$ are shown below.

$$\mathbf{u}^* = \mathbf{u}^n + dt\mathbf{H}^n, \tag{33}$$

$$\mathbf{u}^{n+1} = \mathbf{u}^n + dt\mathbf{H}^n - \frac{dt}{\rho}\nabla p. \tag{34}$$

The divergence of the difference between (33) and (34) gives the Poisson equation for the pressure,

$$\nabla \cdot \nabla p = \frac{\rho}{dt}\nabla \cdot \mathbf{u}^*. \tag{35}$$

This equation is identical to the one obtained from taking the divergence of the momentum equation. Thus the pressure found in (35) is essentially the pressure at time t_n. Once the solution of pressure is obtained, the divergence-free velocity field can be recovered by

$$\mathbf{u}^{n+1} = \mathbf{u}^* - \frac{dt}{\rho}\nabla p. \tag{36}$$

The new velocity is divergence free and its vorticity is equal to that of the provisional velocity because,

$$\nabla \times \mathbf{u}^{n+1} = \nabla \times \mathbf{u}^* - \frac{dt}{\rho}\nabla \times \nabla p = \nabla \times \mathbf{u}^*. \tag{37}$$

In this derivation, the projection method and the pressure-Poisson method are essentially the same. They will go separate ways when the approximations of gradient and divergence are introduced. Suppose discrete divergence operators **D** and **G** are used to approximate the divergence and gradient, respectively. Then the discrete form of Eq. (35) is

$$\mathbf{DG}p = \frac{\rho}{dt}\mathbf{D}\mathbf{u}^*. \tag{38}$$

The projection method adheres to this derivation and the discrete Laplacian is given by **L = DG**. The Laplacian in pressure-Poisson formulation represents the minimization which is not related to the Navier–Stokes equations and thus any discrete Laplacian will suffice. Solving Eq. (38) by a direct method and correcting the velocity using the respective discrete gradient will result in a machine accurate divergence. Using a Laplacian operator other than this one will leave a significant divergence in the velocity fields, even when solved with a direct method. When the Poisson equation is solved by iterative methods, pressure-Poisson formulations need to recalculate the divergence and then start the iteration again. On the other hand, projection methods only need to compute the divergence once. Therefore the projection method offers a clear computational advantage over the pressure-Poisson formulation when aiming at small mass-conservation errors. The projection operator deriving the method's name is defined as

$$\mathbf{P} = \mathbf{I} - \mathbf{G}(\mathbf{DG})^{-1}\mathbf{D}.$$

The derivation shown here is equivalent to the Helmholtz–Hodge decomposition in [23] which states that any vector field $\mathbf{u}^*$ can be uniquely decomposed into two orthogonal fields: **u** a divergence-free field and ∇p a gradient of a potential field.

However, it should be noted that the projection method does not conserve the L_2-norm of the provisional velocity. Let $(\cdot,\cdot)$ be a scalar product of two vectors, the L_2-norm of the Helmholtz–Hodge decomposition is given by

$$(\mathbf{u}^*, \mathbf{u}^*) = (\mathbf{u}, \mathbf{u}) + (\nabla p, \nabla p) + 2(\nabla p, \mathbf{u}).$$

Because the two components are orthogonal, the third term on the r.h.s. vanishes and we have

$$(\mathbf{u}^*, \mathbf{u}^*) = (\mathbf{u}, \mathbf{u}) + (\nabla p, \nabla p),$$
$$(\mathbf{u}^*, \mathbf{u}^*) \geqslant (\mathbf{u}, \mathbf{u}).$$

If the divergence-free field **u** were to have the same L_2-norm as $\mathbf{u}^*$, the ∇p and **u** cannot be orthogonal which is against the underlying concept of projection methods. This equation indicates that the energy is strictly decreasing, when the provisional velocity was not divergence-free. This fact is used by Chorin [24] to show the stability of the projection method. Therefore the projection method is stable, but not energy-conserving. Even if the numerical scheme for the momentum equation was energy conserving, a reduction in L_2 norm of the momentum can be expected.

In fourth-order context, we have the freedom to use second-order or fourth-order approximations for **D** and **G**. This leads to four possible choices of the Laplacian namely (i) $\mathbf{D}_2\mathbf{G}_2$, (ii) $\mathbf{D}_2\mathbf{G}_4$, (iii) $\mathbf{D}_4\mathbf{G}_2$ and (iv) $\mathbf{D}_4\mathbf{G}_4$. The first and the fourth Laplacian are formal second-order and fourth-order, respectively. The other two are non-formal. In an existing second-order code, the second-order projection method ($\mathbf{D}_2\mathbf{G}_2$) is usually implemented. On staggered grids this $\mathbf{D}_2\mathbf{G}_2$ is a well known 7-points Laplacian which can be solved in a very efficient way. The most important question here is whether $\mathbf{D}_2\mathbf{G}_2$ is sufficient to deliver a fourth-order accurate solution of the velocities. In this paper we restrict the study to the two formal Laplacians. In-depth investigation of these four Laplacians will be reported elsewhere.

4.1. Discretisation of Poisson equation

On uniform grids, the component in x direction of the fourth-order Laplace operator given by the projection method reads

$$\frac{\partial^2 [p]^{xyz}_{i,j,k}}{\partial x^2} = \frac{[p]^{xyz}_{i\pm3,j,k} - 54[p]^{xyz}_{i\pm2,j,k} + 783[p]^{xyz}_{i\pm1,j,k} - 1460[p]^{xyz}_{i,j,k}}{576}. \tag{39}$$

On non-uniform grids it is convenient to construct the Laplacian from the matrices D_{4x} and G_{4x} which are the approximations of the cell-averaged values of divergence and gradient, respectively. They are given by

$$D_{4x} = \frac{I_c(is) - I_c(is-1)}{xs(is) - xs(is-1)} \quad \text{and } G_{4x} = \frac{I'_c(i+1) - I'_c(i-1)}{x(i+1) - x(i)},$$

where I_c and I'_c are the cell-centered deconvolutions defined in Eqs. (11) and (12), respectively. The consistent Laplacian operator in x-direction is simply given by $L_{4x} = D_{4x}G_{4x}$ and the three-dimensional Laplacian is

$$\mathbf{L}_4 = D_{4x}G_{4x} + D_{4y}G_{4y} + D_{4z}G_{4z}, \tag{40}$$

which leads to 19-point stencil. In this work, we use a direct method that uses fast Fourier transformations in the periodic directions and the Gaussian elimination in the wall-normal direction. After solving the Poisson equation, the divergence-free velocity is recovered by Eq. (36) with the respective discrete gradient. In general cases, the grid spacing may not be uniform and the FFT will not work. Since the residual obtained from the discrete Laplacian given by the projection method is the mass imbalance in the flow field, one can simply compute the residual using Eq. (40) and solve the equation by a relaxation method such as Stone's strongly implicit procedure [25]. It was shown in [26] that the divergence-free approximate projection method can further reduce the number of stencil points of the discrete Laplacian to 13 without degrading the accuracy of the solution. The performance of an iterative Poisson solver with this approach was shown in [27] to be 15% slower than the direct method used in this work for the divergence at the order of $10^{-5}u_b/H$.

5. Boundary closures

Near the boundary we cannot use all of the formula proposed earlier due to lack of information outside the domain. Either asymmetric stencils, a certain kind of extrapolation or lower-order stencils must be used. Carpenter et al. [28] pointed out that high-order closures might be unstable in a finite difference context. For example, the fourth-order scheme must be closed with third-order closure to ensure stability. In finite volume context, Kobayashi [4] reported that the fourth-order closure is necessary for a fourth-order global accuracy. Neumann boundary conditions are intensively studied in his work. In this section we consider the treatment of the solid surface as a Dirichlet boundary condition depicted in Fig. 4. Approximation stencils near solid surfaces should not extend too much into the inner domain because the strong differences in the velocity gradient near the wall and in the inner domain decrease the accuracy. The compact fourth-order schemes require only the two nearest cells at the boundary thus it is less sensitive to this problem compared to the explicit fourth-order scheme.

5.1. Closures for collocated variables

For the deconvolution of collocated variables at the boundary (Fig. 4(a)), the value given by the boundary can be used directly in the deconvolution formula of the inner domain (Eq. (13)). The boundary value can be moved to the right-hand-side and the resulting linear system can be solved by the Thomas algorithm. The only closure needed here is for the differentiation (Eq. (14)). In our work we use a third-order closure at the boundary:

$$\left[\frac{\partial u}{\partial z}\right]^{xy}_{is,j,0s} + 2\left[\frac{\partial u}{\partial z}\right]^{xy}_{is,j,1s} = \frac{3}{2h_z}\left([u]^{xyz}_{is,j,1} + [u]^{xyz}_{is,j,2}\right) - \frac{3}{h_z}[u]^{xy}_{wall}. \tag{41}$$

This closure has the same convergence rate as the differentiation in the inner domain when the grid is not uniform. Thus using this third-order differentiation here does not degrade the global accuracy.

5.2. Closures for staggered variables

The first staggered cell in the domain is half-a-cell far from the boundary (Fig. 4(b)) and the inter-cell deconvolution in Eq. (13) is closed by the following fourth-order approximation:

$$[w]^{xy}_{i,j,1} + \frac{19}{21}[w]^{xy}_{i,j,2} = \frac{11}{7}[w]^{xyz}_{i,j,1s} + \frac{1}{7}[w]^{xyz}_{i,j,2s} + \frac{4}{21}[w]^{xy}_{i,j,wall}. \tag{42}$$

The third-order closure for the differentiation in Eq. (14) is

$$\left[\frac{\partial w}{\partial z}\right]^{xy}_{i,j,1} - \frac{11}{13}\left[\frac{\partial w}{\partial z}\right]^{xy}_{i,j,2} = \frac{36}{23h}[w]^{xyz}_{i,j,1s} - \frac{12}{23h}[w]^{xyz}_{i,j,2s} - \frac{24}{23h}[w]^{xy}_{i,j,wall}. \tag{43}$$

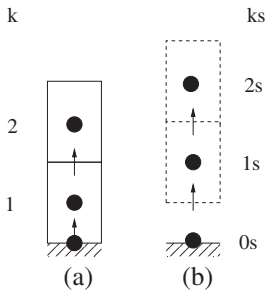

Fig. 4. Arrangement of the closure stencils near the Dirichlet boundary condition: (a) compact differentiation of collocated variables and (b) compact deconvolution and differentiation of staggered variables. Solid rectangles are the collocated cells (u) and dashed rectangles are staggered cells (w). Known values are shown by the circles and the arrows represent the position of the approximated surface-averaged values.

It is noteworthy that using deconvolved values for the differentiation is not recommended even though its asymptotic errors are fourth-order. The nth order leading truncation term of the deconvolution transfers into $(n-1)$th order for the differentiation thus using them for the differentiation does not improve the accuracy.

In the cell-centered deconvolution and the approximation of convective velocities, we simply set the velocity to the wall value, for example zero in the case of a no-slip wall. The pressure cell within the wall is assumed to be equal to the pressure at the first cell in the domain. This ensures a second-order accurate enforcement of $\frac{\partial p}{\partial n} = 0$ at the wall. A similar extrapolation is also used by Verstaapen and Veldman [21]. These treatments are sufficient for the fourth-order convergence which will be shown numerically in Section 7.

6. Analysis

The accuracy of the NSE solver is determined by every single approximation step in the code. It is important to understand how large the errors are being generated in each term. Fourier analysis provides us with a quantitative error for each wave number. The convective and diffusive terms used in this paper have been studied already in [4,6]. In this section we perform a comparative study of numerical errors in the Fourier space. The fourth-order compact deconvolution, compact differentiation, and cell-centered deconvolution are compared.

6.1. Comparative fourier analysis of linear terms

In finite difference context, Fourier analysis of the discretisations of convective and diffusive terms lead to the study of the modified wave number k^* and the modified k^{2^*}, respectively. In finite volume context, where the PDEs are integrated, the quantifications of the accuracy in Fourier space leads to the modified amplitude and modified wave number. These two quantities provide us a great deal of information. However, they cannot be directly compared. A better measurement for comparison is the transfer function where the approximated value is normalized by the exact one. In this section we use the concept of transfer function to compare each approximation in the momentum equation as well as the mass conservation equation.

In order to perform a Fourier analysis of a periodic function $u(x)$ over the domain $[0,L]$, the function $u(x)$ is decomposed into its respective Fourier components. We use a scaled wave number, $kh \in [0,\pi]$, similar to [2] and each Fourier component is given by $\hat{u}_k exp(ikh)$. The model equation we consider here is the one-dimensional transport equation in a periodic domain described by

$$\frac{\partial u}{\partial t} + c\frac{\partial u}{\partial x} = \Gamma \frac{\partial^2 u}{\partial x^2}. \tag{44}$$

The finite volume discretisation of the above equation is

$$\frac{1}{\Omega}\frac{\partial \bar{u}_i}{\partial t} + c[\tilde{u}_{i+1/2} - \tilde{u}_{i-1/2}] = \Gamma\left[\left.\widetilde{\frac{\partial u}{\partial x}}\right|_{i+1/2} - \left.\widetilde{\frac{\partial u}{\partial x}}\right|_{i-1/2}\right]. \tag{45}$$

In this one-dimensional problem we use the overbar to represent cell-averaged values and the approximations are represented by tilde symbol. Projecting the above equation in the Fourier space, we obtain the following equation for each wave-number k:

$$\frac{\partial \hat{\tilde{u}}_k}{\partial t} + ickT_I(k)\hat{\tilde{u}}_k = -\Gamma k^2 T_D(k)\hat{\tilde{u}}_k. \tag{46}$$

The transfer function of an approximation is defined by the ratio of the approximated value over the exact value, for example $T_I(k) = \hat{\tilde{u}}_k/\hat{u}_k$ defines the transfer function of a deconvolution. The transfer function of the differentiation is defined equivalently. The overall accuracy of a numerical solution of the transport equation is determined by T_I and T_D. For the purpose of a general analysis, let $c = \Gamma = 1$ such that only errors of the approximations are considered.

The transfer functions of the cell-centered deconvolution (Eq. (11)), inter-cell deconvolution (Eq. (13)) and the differentiation (Eq. (14)) are plotted in Fig. 5. The significant improvement of the compact fourth-order deconvolution over the second-order is clearly shown. During the projection step, the mass fluxes are computed by the cell-centered deconvolution (Eq. (11)). According to Fig. 5, the second-order cell-centered deconvolution (mid-point rule) is less accurate than the fourth-order inter-cell deconvolution (Eq. (13)), especially for $0.5 < kh < 2$. When the mid-point rule was used to enforce the mass conservation, the errors of the wave components in this range will remain in the velocity fields and thus degrade the level of accuracy that was achieved by the compact fourth-order. The fourth-order cell-centered deconvolution (Eq. (13)) is more accurate than the compact fourth-order inter-cell deconvolution through out the Fourier space.

The discussed cell-centered deconvolutions are used for the mass conservation and the pressure gradient in staggered grid arrangement. According to Fig. 5, we could expect that these approximations will not reduce the accuracy of the compact scheme. *Therefore we do not need compact deconvolutions for the approximations of mass and pressure fluxes in staggered grids*. On the other hand, it is clear that in collocated grids the compact scheme must be used for the approximations of mass

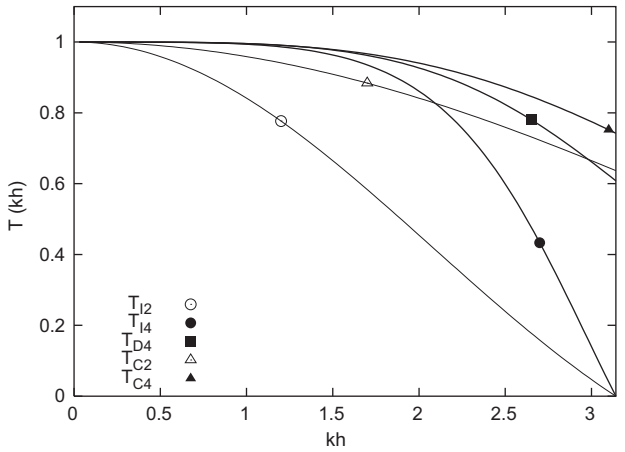

Fig. 5. Comparison of the transfer function of standard second-order and higher-order schemes: second-order inter-cell deconvolution (T_{I2}), fourth-order compact inter-cell deconvolution (T_{I4}), fourth-order compact differentiation (T_{D4}), second-order cell-centered deconvolution (T_{C2}) and fourth-order cell-centered deconvolution (T_{C4}).

and pressure fluxes. Otherwise the accuracy will be limited to that of the explicit scheme. This finding thus has a very important consequence because these two explicit stencils (Eqs. (11) and (12)) lead to a narrow banded Laplacian which can be solved much easier than the full one which would arise when using implicit scheme for D or G like in [11,13].

With this analysis, we can also explain why the second-order solution of pressure on collocated grids strictly limits the accuracy to second-order as reported in [11]. This limitation is, however, less severe on staggered grids. It will be shown later in Section 7 that, on staggered grids a convergence rate of approximately third-order can be achieved with the second-order solution of pressure.

6.2. Fourier analysis of nonlinear terms

Let us consider the fourth-order approximation of the nonlinear convective flux on the East surface of the u-momentum:

$$[\mathrm{u}u]^{yz}_{i+1,j,k} = C2 + N_i, \tag{47}$$

where $C2 = [\mathrm{u}]^{yz}_{i+1,j,k}[u]^{yz}_{i+1,j,k}$, the second-order approximation of the nonlinear convective term. There are several straight forward methods which can be used to compute the nonlinear correction, N_i. In this study we consider three forms for the correction term $\frac{\Delta z^2}{12}\frac{\partial f}{\partial z}\frac{\partial g}{\partial z}$ in Eq. (30):

$$N_1 = \frac{1}{48}\left([u]^{yz}_{i+1,j,k+1} - [u]^{yz}_{i+1,j,k-1}\right)^2. \tag{48}$$

$$N_2 = \frac{1}{192}\left(\left([u]^{xyz}_{is,j,k+1} + [u]^{xyz}_{is+1,j,k+1}\right) - \left([u]^{xyz}_{is,j,k-1} + [u]^{xyz}_{is+1,j,k-1}\right)\right)^2. \tag{49}$$

$$N_3 = \frac{1}{192}\left(\left[\frac{\partial u}{\partial z}\right]^{xy}_{is,j,ks} + \left[\frac{\partial u}{\partial z}\right]^{xy}_{is+1,j,ks} + \left[\frac{\partial u}{\partial z}\right]^{xy}_{is,j,ks+1} + \left[\frac{\partial u}{\partial z}\right]^{xy}_{is+1,j,ks+1}\right)^2 \tag{50}$$

The first correction uses surface-averaged values, the second equation uses cell-averaged values and the third equation averages the first-derivatives provided by the compact differentiation. The nonlinear correction term is analysed using an ansatz function $u(x,z) = exp((i + 0.4)kx + \alpha z)$. This function mimics an oscillating velocity under an exponential gradient in z-direction and its amplitude is varied in x-direction. The cell-averaged values here are treated as exact and surface-averaged values used for $C2$ are fourth-order accurate. The interpolated terms are computed by multiplying the analytical value with the modified amplitude of this ansatz function.

Instead of looking at the whole nonlinear convective term, we consider here just the transfer function of the correction term. The norm of the error, $L_2(|1 - T(N_i)|)$ over $kh \in [0, \pi/2]$ is shown in Table 1. The first row is the norm of the analytical correction, and at the same time the error when we do not apply any correction. According to the table, nonlinear corrections improve the accuracy when the gradient is not too high and they are able to predict roughly two digits of the correction term. The correction using face-averaged values (N_1) is more accurate than the one using cell-average values (N_2). This is attributed to the inferior transfer functions of second-order approximations. The third form (N_3) is slightly more accurate than the second form (N_2) at the lowest gradient, but it performs poorly otherwise. Thus computing the nonlinear correction using face-averaged values is recommended.

Table 1
Square root of L_2-norm of errors of the correction term ($\|N_{exact} - N_i\|_2$) over $kh \in [0, \pi/2]$.

Nonlinear correction form	$\alpha = 0.5$	$\alpha = 1.0$	$\alpha = 1.5$
Without correction	2.7E−2	1.1E−1	2.7E−1
N_1	2.2E−3	4.4E−2	2.9E−1
N_2	3.9E−3	5.3E−2	3.2E−1
N_3	3.3E−3	8.4E−2	4.3E−1

7. Results and discussion

In this section the proposed scheme is evaluated using standard test cases with increasing complexity. First we evaluate each approximation in the NSE using a priori testing. The full discretisation of the NSE is validated in a doubly-periodic shear layer. Treatments of the boundary conditions are evaluated using the instability of plane channel flow. Finally, the practical use of the proposed scheme is demonstrated by direct numerical simulations of turbulent channel flow. The accuracy and efficiency of the scheme are compared to the second-order scheme.

In all simulations, the time-integration is performed by the third-order Runge–Kutta scheme of [29] and the continuity is enforced at every sub-step. This time integration is third-order accurate for both velocity and pressure. The nonlinear correction and fourth-order solution of the pressure are always used except when stated otherwise.

7.1. A priori test

A simple Gaussian function $u(x) = 0.5exp\left(-ln(2)\frac{x^2}{9}\right)$ as proposed in [30] is used as our test function. The domain is set to $[-20,20]$ such that errors at both ends do not affect the global accuracy. We initialize the cell-averaged values analytically and numerical approximations are computed from these cell-averaged values. In this test we consider fourth-order deconvolutions (Eqs. (11) and (13)), the fourth-order differentiation (Eq. (14)) and the fourth-order nonlinear correction with Eq. (48). The errors of these approximations are investigated and plotted in Fig. 6 in which second and compact sixth-order deconvolutions are presented for comparison. In this test case, the error graphs of every scheme are oscillating because they are strongly dependent on the sampling position. Therefore, only the error on even number of cells are plotted for clarity. According to the figure, the error of the second-order inter-cell deconvolution ($I2$) is roughly four times larger than that of the cell-centered ($C2$). The fourth-order inter-cell approximations ($I4, D4$) are comparable to the cell-centered deconvolution ($C4$) on large number of grid cells. The cell-centered deconvolution ($C4$) is the most accurate in general among the fourth-order approximations. The sixth-order compact scheme ($I6$) is better than the compact fourth-order scheme ($I4$). However, the compact sixth-order scheme ($I6$) (from [4]) is only significantly better than $C4$ only when $n > 20$. At this resolution, approximately 8 cells are used to represent the Gaussian bump ($x \in [-8,8]$).

7.2. Doubly-periodic shear layer

In order to expose the role of the pressure, we use a doubly periodic shear layer as the next test case. This simple 2D flow contains Kelvin–Helmholtz instabilities in which the shear layer is perturbed by a sinusoidal disturbance that leads to a

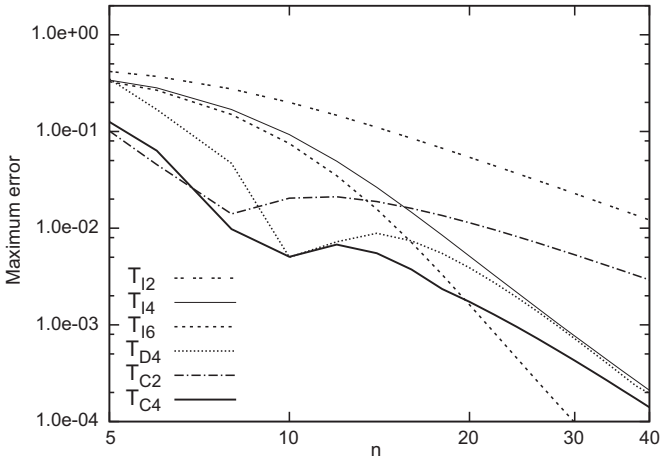

Fig. 6. Convergence of numerical approximations for Gaussian functions (only even number of grid cells are plotted).

roll-up of the vortex sheet into a cone-like shape. The domain $\Omega = [0,1]^2$ is taken for this study and the initial velocities are given by

$$u = \begin{cases} tanh(\sigma(y - 0.25)) & \text{for y } \leqslant 0.5, \\ tanh(\sigma(0.75 - y)) & \text{for y } > 0.5. \end{cases} \tag{51}$$

$$v = \varepsilon\, sin(2\pi x). \tag{52}$$

This flow is governed by three parameters, the shear layer width parameter σ, the perturbation magnitude, ε and the Reynolds number. In this study the Reynolds number based on the maximum velocity and the length of the computational domain is set to 10,000, the shear layer parameter and the perturbation magnitude are 30 and 0.05, respectively. This setting is similar to a *thick shear-layer problem* studied in [31]. In order to show that the proposed scheme converges towards the correct solution, we generate a reference solution of this case on a 512^2 grid using a pseudo-spectral code. In this code, the computation is performed on the physical space and the derivatives are computed using FFT differentiations while the divergence form is used for the convective term.

We provide a qualitative overview of the solutions using the contour plots of the vorticity in Fig. 7. The improvement of the fourth-order over the second-order scheme is clearly visible. At the lowest resolution, the fourth-order solution preserves the correct shape of the vortex sheet while it is already distorted in second-order solution. The fourth-order has more wiggles but their magnitudes are smaller than those of the second-order. When the resolution is doubled, numerical wiggles are still disturbing the second-order solution. On the other hand, the solution of the fourth-order scheme is already smooth and the numerical wiggles at this resolution are comparable to those on the finest solution (256^2) of the second-order scheme. In this figure we see that even on the coarsest grid which is heavily under-resolved, the fourth-order scheme still delivers an appreciable solution unlike the second-order scheme.

The maximum errors of the fourth-order schemes and the convergence rates with respect to the reference solution are shown in Table 2. In this convergence study we transfer the pointwise value of the reference solution to the cell-averaged ones using seventh-order integration and cubic spline interpolation. Here we compare the two formulations of the convective velocities. On coarse grids, *T*4 is slightly more accurate than *DF*4. This is because the leading truncation term of *T*4 is smaller. The convergence rates of these two formulations approach fourth-order when the grid is sufficiently fine. The differences between the solutions using a different convective velocity are very small and the solutions are visually indistinguishable. For this reason, only the results from *DF*4 were shown in Fig. 7.

We repeat the simulation again, but with second-order solution of pressure, i.e. the divergence and the pressure gradient are computed with second-order schemes and the discrete Laplacian is $\mathbf{D}_2\mathbf{G}_2$. The result is given in Table 3 for the *T*4 convective velocity. The effects of the second-order pressure can be observed at every grid size. The convergence rate of the L_∞-norm falls between second- and third-order. The convergence rate of the L_2-norm tends to third-order. At low resolution, the errors primarily stem from the wiggles inherit in the approximation of the convective term and therefore we see little differences between second-order and fourth-order pressure. Once the wiggles have disappeared ($N \geqslant 196^2$), the error of the solution using second-order pressure is significantly larger.

To explore the stability of the proposed scheme, we performed inviscid simulations using the same initial conditions on 128^2 grid and advance the flow in time for 10 through flows. The L_2 norms of the cell-averaged velocities that is commonly considered as the discrete kinetic energy are plotted in Fig. 8(a) for three CFL numbers. First the discrete kinetic energy is increased by 0.05 per mille and then declined. When the time step size is reduced, the reduction of the energy in the second part ($t > 0.8$) gets smaller suggesting that the reduction in the kinetic energy in the second part comes from the dissipative property of the third-order Runge–Kutta time-integration. The increase of the kinetic energy in the first part however dose not change with the time step size which indicates that this increase is associated with the spatial scheme. We analyze the discrete convective matrix $C(\mathbf{u})$ in the inviscid flow equations i.e. $\mathbf{u}_t + C(\mathbf{u})\mathbf{u}$. This convective matrix comprises of the convective velocity and the interpolation matrix of the momentum (see [21]). The diagonal elements of $C(u)$ of the proposed algorithm are exactly zero, but the off-diagonal elements are not skew-symmetric which leads to small errors in the energy conservation. The level of this error is small, and is comparable to the divergence form of the convective term investigated in [13]. Fig. 8(a) also indicates that the error in the energy conservation is significantly lower than the error of the time-integration at the practical CFL numbers (CFL = 0.25 and 0.5). Even though this flow is inviscid and the grid is highly underresolved (shown by flat energy spectra in Fig. 8(b)), the proposed algorithm does not blow up after a long integration time. In finite difference discretisation, Knikker[13] was able to demonstrate the energy conservation on uniform grid. To the best of our knowledge, the energy conservation for compact scheme in finite volume context is still an open issue. The test we made here demonstrate that energy conservation is violated only to a very small degree and that long term stable solutions could be achieved without any further stabilization or regularization.

7.3. Instability of plane channel flow

The instability of plane channel flow is a common test case used to validate higher-order accuracy of numerical schemes. In this test case, the parabolic profile of the channel flow is disturbed by the most unstable eigenfunction. The solution of the velocity fields can be described by the Orr–Sommerfeld equation:

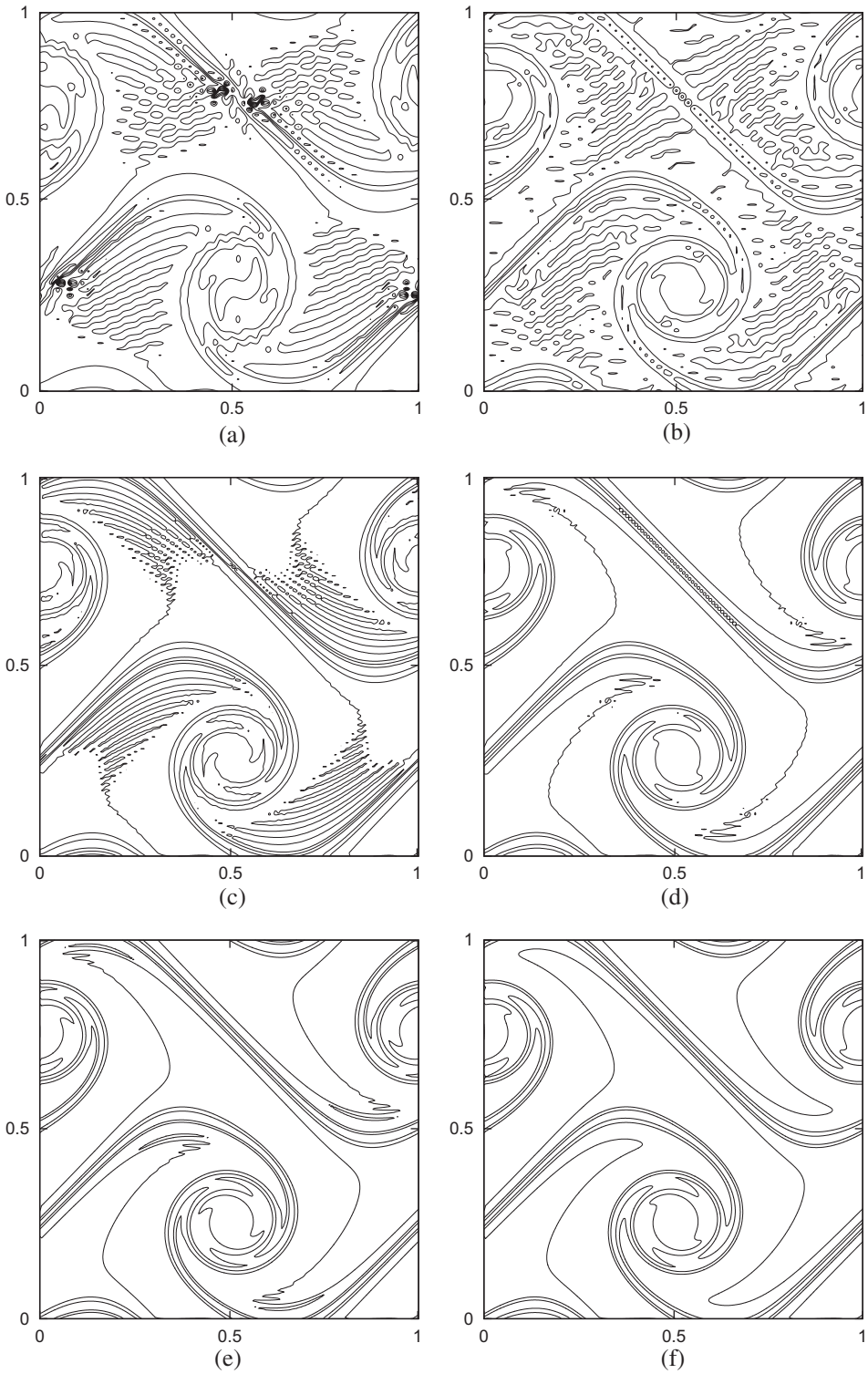

Fig. 7. Contour plot of vorticity from −36 to 36. Left: second-order, Right: fourth-order (DF4). The resolution are 64^2, 128^2 and 256^2 from top to bottom.

$$u(x,y,t) = (1-y^2) + \varepsilon\mathcal{R}\rceil\dashv\updownarrow\left(\Psi(y)e^{i(\alpha x-\omega t)}\right) \tag{53}$$

$$v(x,y,t) = -\varepsilon\mathcal{R}\rceil\dashv\updownarrow\left(\alpha i\Psi\left((y)e^{i(\alpha x-\omega t)}\right)\right). \tag{54}$$

Table 2
Maximum error of the streamwise velocity and its convergence rate of T4 and DF4 convective velocities using fourth-order solution of pressure at $t = 1.2$, in doubly periodic shear layers flow.

N	$\|\varepsilon\|_\infty$ of u		Convergence rate	
	T4	DF4	T4	DF4
64^2	2.5835E−02	2.7744E−02	–	–
96^2	1.0762E−02	1.1147E−02	2.16	2.25
128^2	4.4665E−03	5.0558E−03	3.06	2.75
196^2	8.9431E−04	1.2273E−03	3.97	3.49
256^2	2.6394E−04	2.5998E−04	4.24	5.39

Table 3
Error and the convergence rate of the streamwise velocity at $t = 1.2$ using *DF*4 convective velocities and second-order solution of pressure ($\mathbf{D_2G_2}$).

N	Error of u		Convergence rate	
	$\|\varepsilon\|_\infty$	$\|\varepsilon\|_2$	L_∞	L_2
64^2	3.23E−02	1.36e−01	—	—
96^2	1.22E−02	1.03e−01	2.4	2.7
128^2	5.54E−03	8.32e−02	2.7	2.7
196^2	2.02E−03	5.93e−02	2.5	2.8
256^2	1.02E−03	4.57e−02	2.4	2.9

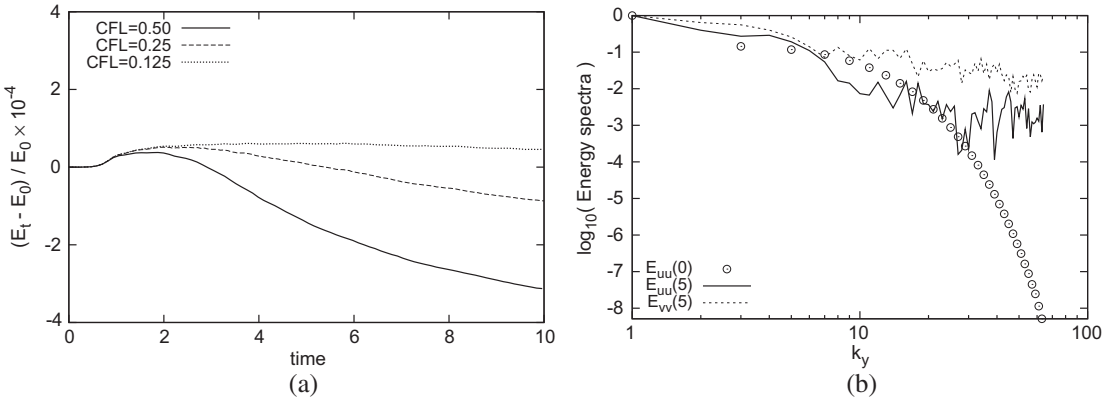

Fig. 8. (a) Evolution of the normalized kinetic energy error in the doubly periodic shear layer flow. (b) One-dimensional Energy spectra in y-direction at t equal to 0 and 5 along $x = 0.5$.

The energy of the perturbation and its growth-rate is computed by:

$$E_d(t) = \int_\Omega \left((u(x,y,t) - u(x,y,0))^2 + (v(x,y,t) - v(x,y,0))^2 \right) dxdy, \tag{55}$$

$$G_p(t) = 2\omega_i = 2ln\left(\frac{\partial E_d(t)}{\partial t}\right). \tag{56}$$

The Orr–Sommerfeld eigenfunction $\Psi(y)$ here is a stream function and only the real part of the perturbation is taken into the velocities. This test-case is sensitive to the balance among the terms in the Navier–Stokes equations. The viscous term attenuates the perturbation while the convective term transfers energy from the main flow to the perturbation. If the approximation of the diffusion term is accurate and the convective term is under approximated, the growth-rate of the disturbance will be less than the analytical one. This is a common situation found in finite difference methods applied to this case [14,32–35]. On the other hand, the growth-rate will be larger than the analytical one when the situation is reverse. Higher-order convergence can only be achieved if every approximation is correctly treated. Therefore this is a formidable test case for numerical schemes and the boundary closures. The conditions of this test are set to the same conditions used in [32] where $Re = 7500$, $\alpha = 1$, $\varepsilon = 0.0001$ and the only unstable mode is $\omega = 0.24989154 + 0.00223498i$. The expected analytical growth rate is $G_p(t) = 4.46996\text{E}{-}03$. The computational domain is $[L_x, L_y] = [2\pi H, 2H]$ based on the channel half-width

H. The CFL is kept constant at 0.05 such that the errors are dominated by the spatial approximations. The simulations are calculated using double precision and the growth-rate of the perturbation is measured at $t = 50.29H/U_c$ where U_c is the velocity at the center of the channel.

Our grid dependency study shows that $N_x = 32$ is sufficient to conduct a convergence study in y-direction with the fourth-order scheme. In order to be on the safe side the results in Tables 4 and 5 are computed using $N_x = 64$. Table 4 shows a clear convergence towards fourth-order for both formulations of convective velocities on uniform grids. A fourth-order convergence rate on non-uniform grids is shown in Table 5. The smallest grid spacing on these grids is set to $1/N_y$ (half-size of the uniform grid). The predictions of the growth-rates on non-uniform grid are comparable to those on uniform grids with twice the number of grid cells. Both formulations of convective velocities deliver a comparable level of accuracy.

We further use this case to study the role of the nonlinear correction. To this end, we plot in Fig. 9(a) the time evolution of the perturbation energy for two grid resolutions with and without nonlinear correction. The figure shows that the nonlinear correction facilitates additional energy transfer to the perturbation bringing the growth-rate closer to the analytical one. On the coarse grid, the nonlinear correction is helpful, but not as impressive as on the fine grid. It has to be noted that a growth-rate higher than the analytical one does not imply an instability of the numerical scheme. It means that the perturbation is gaining more energy from the mean field than what is lost by the dissipation. In fact, the total kinetic energy of the system is reducing in all cases shown there.

Several grid systems in the wall-normal directions have been used to simulate this flow. Chebychev grids are used in [32] and geometric grids are used in [14,33]. The geometric grids deliver better results at a much lower number of grid points. Further, the Chebychev grid does not offer flexibility in grid placement. In this test case, the spatial gradient of the perturbation varies greatly. The grid cells should be distributed in a way that the errors over the whole region are comparable. The effects of the grid distribution in the wall-normal directions are shown in Fig. 9(b) where we plot the perturbation growth

Table 4
Convergence study in y-direction of the instability of plane channel flow on *uniform* grid with $N_x = 64$. The table shows growth-rates of perturbations (G_p), their errors (ε_p) and the corresponding convergence rates (C_a).

N_y	$G_p(T4)$	$G_p(DF4)$	$\varepsilon_p(T4)$	$\varepsilon_p(DF4)$	$C_a(T4)$	$C_a(DF4)$
32	9.66E−03	1.09E−02	5.19E−03	6.44E−03	–	–
64	6.34E−03	6.37E−03	1.88E−03	6.44E−03	1.46	1.76
128	4.66E−03	4.65E−03	1.90E−04	1.78E−04	3.31	3.42
256	4.48E−03	4.47E−03	1.08E−05	1.41E−06	4.13	6.97
512	4.47E−03	4.47E−03	7.37E−07	3.19E−08	3.88	5.47

Table 5
Convergence study in y-direction of the instability of plane channel flow on *non-uniform* grid with $N_x = 64$.

N_y	$G_p(T4)$	$G_p(DF4)$	$\varepsilon_p(T4)$	$\varepsilon_p(DF4)$	$C_a(T4)$	$C_a(DF4)$
32	5.919E−03	6.432E−03	1.45E−03	1.96E−03	–	–
64	4.628E−03	4.646E−03	1.58E−04	1.76E−04	3.20	3.48
128	4.475E−03	4.485E−03	4.55E−06	1.52E−05	5.12	3.53
256	4.470E−03	4.470E−03	1.91E−07	4.35E−07	4.57	5.06

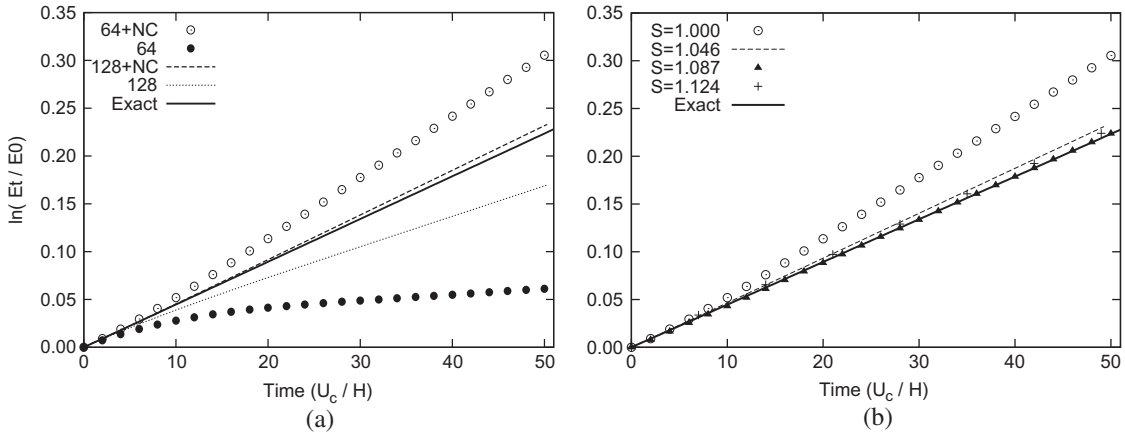

Fig. 9. (a) Time evolution of the perturbation energy on: (a) two uniform grids and (b) non-uniform grids with different stretching factor (S). All grids are computed with $N_x = 64$. On uniform grid, the resolution in the wall-normal direction of the two grids are $N_y = 64$ and 128 and the result with nonlinear correction are denoted by 64 + NC and 128 + NC while the result without the nonlinear correction are denoted by 64 and 128.

rate on four different grid distribution with the same number of grid cells ($N_x = 32$ and $N_y = 64$) on the same scale as the previous figure. The uniform grid ($S = 1.000$) and the non-uniform grid with $S = 1.046$ are the ones reported in Tables 4 and 5, respectively. A stronger stretching ($S = 1.087$) leads to an excellent prediction of the growth rate while the strongest stretching ($S = 1.124$) gives worse result.

In the previous three test cases, we have evaluated the proposed scheme including the boundary closures. A fourth-order convergence rate is obtained in all cases with the fourth-order approximation of pressure. The overall accuracy falls to third-order if the pressure was only treated by a second-order scheme. The nonlinear correction plays crucial role in energy transfer in the instability of plane channel flow. In the next step we investigate the application of the fourth-order scheme in fully turbulent flows.

7.4. Turbulent channel flow: $Re_\tau = 180$

In this section we investigate the accuracy and the performance of the newly developed scheme in turbulent channel flow at $Re_\tau = 180$, based on the friction velocity u_τ. This test case has been employed to study turbulence and its modeling for the past two decades. Results of numerical simulations using spectral codes from several authors [18,36,37] are publicly available for comparison. Numerical simulations using other classes of approximation should converge to these data.

The performance of several higher-order schemes were reported to be comparable to second-order schemes in simulations of turbulent flows. Therefore we carefully investigate the performance of the proposed scheme by evaluating the two choices of convective velocity, performing a grid dependency study and comparing the runtime to the second-order scheme. The parameters of the numerical grids and the computational domain used in this study are listed in Table 6 along with the three spectral simulations which are used for comparison. In our simulations, the streamwise, spanwise and wall-normal directions are set to x, y and z accordingly. The computational box is $[L_x, L_y, L_z] = [12.57H, 4.20H, 2H]$ which is the same domain used in [18]. Homogeneity is assumed in streamwise and spanwise directions and thus periodic boundary conditions are applied. The top and the bottom walls are treated by no-slip boundary conditions. All spatial dimensions in this section are normalized by channel half-width (H) if not stated otherwise. The flow is driven by a constant pressure gradient which is added as a source term in the momentum equation of the streamwise velocity. There is no control of mass flow within the simulations. The driving pressure gradient is balanced only by the shear force on the top and bottom walls. The initial velocity field is obtained from imposing a random perturbation on the logarithmic velocity profile. The criterion of a statistically steady state is assumed when the bulk flow velocity is not changed more than $0.5\%U_b$ over a period of $10Lx/U_b$. After the statistically steady state is reached, the flow is further advanced for $10Lx/U_b$. The sampling is then performed for $100Lx/U_b$ together with the averaging in the homogeneous directions.

This study is organized into four parts. In the first part, we rule out the T4 convective velocity. The accuracy of the proposed scheme with the DF4 convective velocity is demonstrated in the second part, the grid dependency study. In the third part, we evaluate the efficiency of the fourth-order scheme. Its computational cost and accuracy are compared against the second-order scheme. Having identified accuracy and performance of the full scheme, we discuss the necessity of the fourth-order solution of pressure and the influence of the nonlinear correction in the fourth part.

7.4.1. Choice of the approximation of the convective velocities

In laminar flows, the flow fields are usually smooth which was also the case for the flows presented earlier. In all previous simulations, the cell-averaged divergence of the convective velocities was always smaller than $10^{-6}u_{ref}/L$ for the respective characteristic length (L) and velocity (u_{ref}) in those cases. Consequently, the differences between the two alternatives for the convective velocities were negligible. In this section we investigate the behaviour of the two alternatives for the convective velocity, *T*4 and *DF*4 in a turbulent channel flow. In order to exclude other effects, we use uniform grids in every direction and turn off the nonlinear correction. Here, grid A and grid B listed in Table 6 are considered. The convective velocities *T*4 and *DF*4 perform significantly different on the coarse grid but they are comparable on the fine grid (Fig. 10(a) and (b)). According to this graph, the T4 convective velocity should not be used in LES and is probably equivalent to DF4 when the grid is DNS-like. However, the absolute values of the cell-averaged divergence on the u-momentum cell shown in Fig. 10 shifts our favour

Table 6
Specification of numerical grids used in the grid dependency study.

Grid	NX	NY	NZ	Δx^+	Δy^+	Δz^+_{min}	Δz^+_{max}
A	48	42	64	47.2	18.0	5.6	5.6
B	96	64	128	23.6	11.8	2.8	2.8
C	32	32	32	70.7	23.6	5.4	18.6
M1	64	64	64	35.4	11.8	2.7	9.7
M2	96	80	96	23.6	9.4	1.1	5.8
F	128	128	128	17.7	5.9	0.72	4.4
MKM1999 [18]	128	129	128	17.7	5.9	0.054	4.4
KMM1987 [36]	192	129	160	11.9	7.1	0.054	4.4
H2006 [37]	256	256	121	16.9	8.4	0.062	4.7

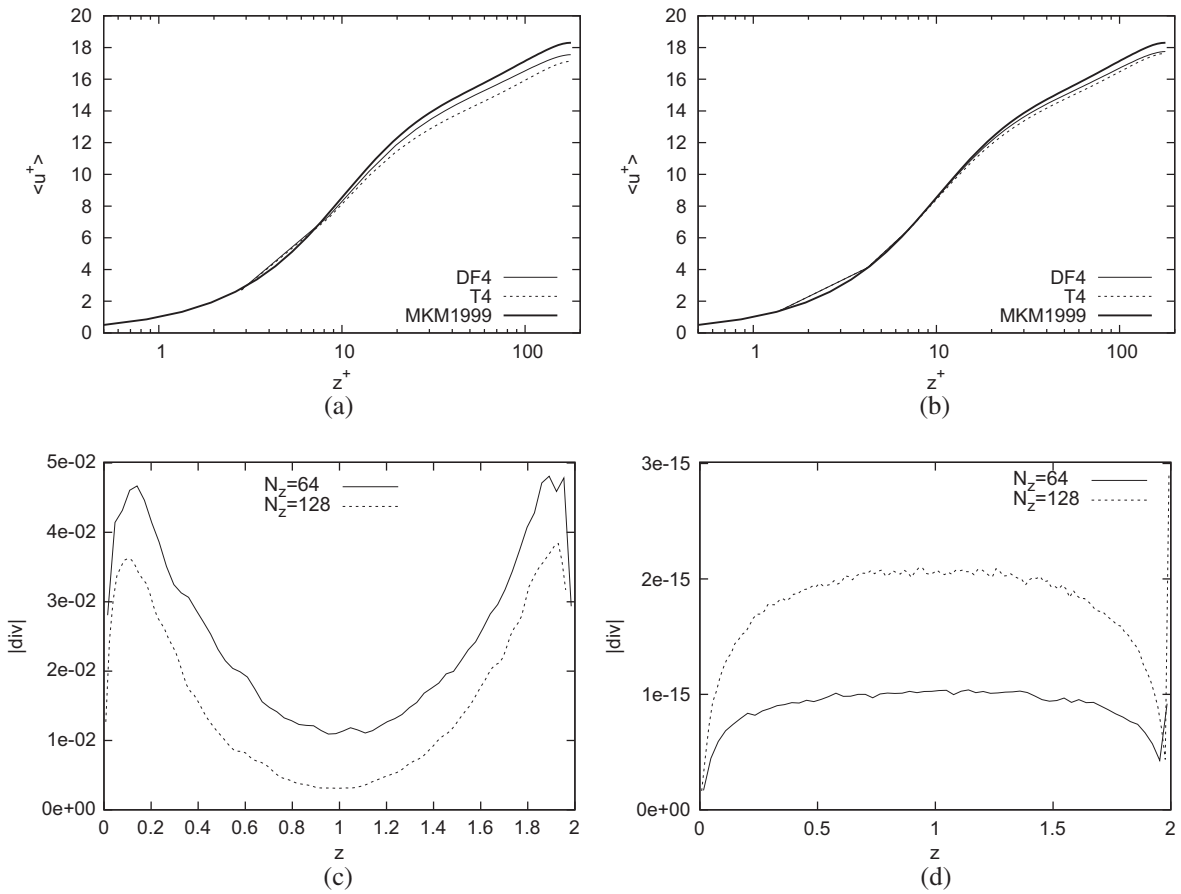

Fig. 10. Mean profiles of streamwise velocity along wall-normal direction of grid A (a) and grid B (b). Averaged mass imbalance per unit volume on u-momentum cells of T4 (c) and DF4 (d).

entirely to DF4. The divergence-free convective velocity conserves mass close to machine accuracy on the momentum cell while the $T4$ formulation creates the maximum cell-averaged divergences of approximately $0.045U_b/H$. This means that an artificial momentum of the comparable amount are being removed or added per unit-momentum (see Eq. (10)). Therefore we choose DF4 to approximate the convective velocities for the remaining tests.

7.4.2. Grid dependency study

In this part, the accuracy of the fourth-order compact scheme is evaluated using grid C to F listed in Table 6. These four grids mimic different situations one may encounter in numerical simulations of turbulent flows. Grid C is on the extreme end of the resolution where one can perform a reasonable LES. $M1$ is too coarse for DNS simulations but an excellent resolution for LES. $M2$ is a reasonable and F is a good resolution for DNS. The grid spacings of grid F match the ones used in [18] in the center of the channel.

The mean flow variables shown in Table 7 demonstrate a convergence towards the spectral solution. The mean bulk and center line velocities clearly converge towards the spectral solution. On the grid C, the bulk flow is underestimated by 6.4% and the error is reduced to 2.3% on $M1$. Results on grid $M2$ and grid F are very close and comparable to the reference solutions.

Table 7
Mean flow variables.

Grid	U_c/u_τ	U_b/u_τ	C_f
C	16.68	14.55	9.35E−3
M1	17.62	15.20	8.57E−3
M2	18.19	15.63	8.20E−3
F	18.34	15.77	8.16E−3
KMM1987 [36]	18.20	15.63	8.18E−3
MKM1999 [18]	18.30	15.52	8.18E−3

Qualitative convergence of the scheme is shown in Fig. 11(a). Amiri et al. [8] incorporated LES into Pereira's fourth-order scheme and found that the result without explicit filtering is poor on the 64^3 grid which is equivalent to $M1$. Here we can obtain a satisfactory result on the same resolution without any filtering or modelling. Increasing resolution from grid $M1$ to grid $M2$ places the profile almost on top of the spectral solution. When this profile is plotted together with two spectral solutions in Fig. 11(b), we see that it is lying between these two. The mean streamwise velocity on grid F is not plotted here because it is lying between the two spectral solutions as well.

In Fig. 11(c) the square-roots of the surfaced-averaged values of the Reynolds normal stresses e.g. $[uu]^{yz}_{i,j,k}$ extracted from the momentum equation are plotted against the two reference spectral solutions. It confirms that the grid $M2$ is sufficient to capture all scales of engineering interest. The Reynolds normal stresses of the fourth-order scheme do not differ from the reference solutions more than the difference between those two. This level of difference is much smaller compared to uncertainties occurring in physical experiments.

Next we consider the higher-order statistics, the skewness and the flatness factors. The Skewness factor shown in Fig. 12(a) confirms the consistency and convergence of the scheme. The profiles of grid $M2$ are satisfactory close to the spectral solution. The profile of $S(u)$ is on top of the reference solution almost everywhere and the profile of $S(w)$ is satisfactory. The value of 0.06 is obtained near the wall compared to -1.3 when the second-order scheme was used (not shown). To the best of our knowledge, all second-order codes predict negative $S(w)$ near the wall when the grid resolution is not finer than those used in [18,36]. Increasing the solution to grid F clearly improves the accuracy of the solutions and brings $S(w)$ on top of the spectral solution. The flatness factors, are plotted in Fig. 12(b). The profiles on both grids are highly satisfactory for the streamwise velocity but notable shortcomings are observed in $F(w)$. The deviations we see here in the skewness and flatness factors can be attributed to small scale structures at the far end of the spectrum. In order to reveal how much the fourth-order scheme is behind the spectral scheme, one-dimensional spectra of the cell-averaged values are investigated and plotted in Fig. 13(a) and (b). In these figures, the Fourier spectra are normalised by the value of the first mode. The energy spectrum E_{uu} in the y-direction on grid C is far from the spectral solution, but the spectra on the other grids follow the one of the spectral code nicely. In the streamwise direction, where the convection is much stronger, the energy spectra on all grids follow the spectral solution up to about 60% of the Nyquist limit and then start to fall sharply. This is consistent with the sharp drop of the transfer function of the fourth-order compact deconvolution used for the convective fluxes shown in Fig. 5.

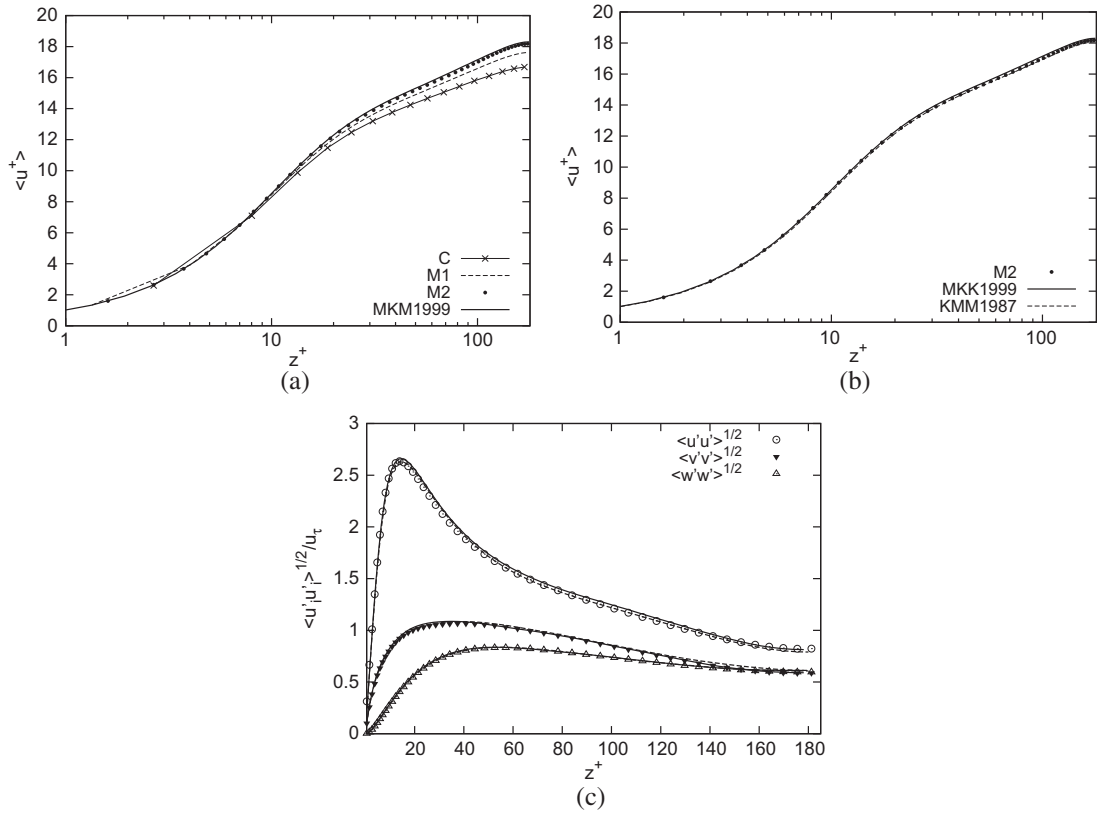

Fig. 11. (a) Convergence of the mean streamwise velocity profile towards the spectral solution from [18]. Profiles of the mean streamwise velocity (b) and the square root of Reynolds normal stresses (c) on grid $M2$ compared to reference solutions from [18] (solid line) and [36] (dashed line).

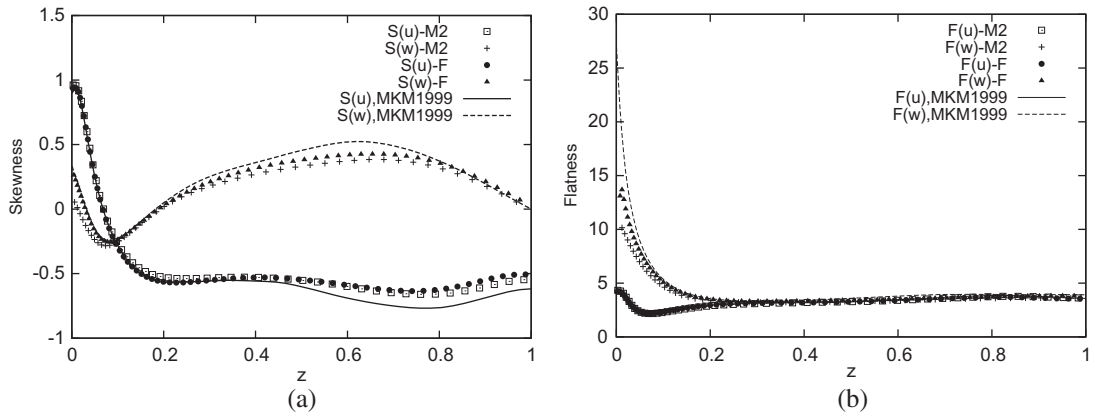

Fig. 12. Skewness factor (a) and flatness factor (b) on grid M2 and grid F.

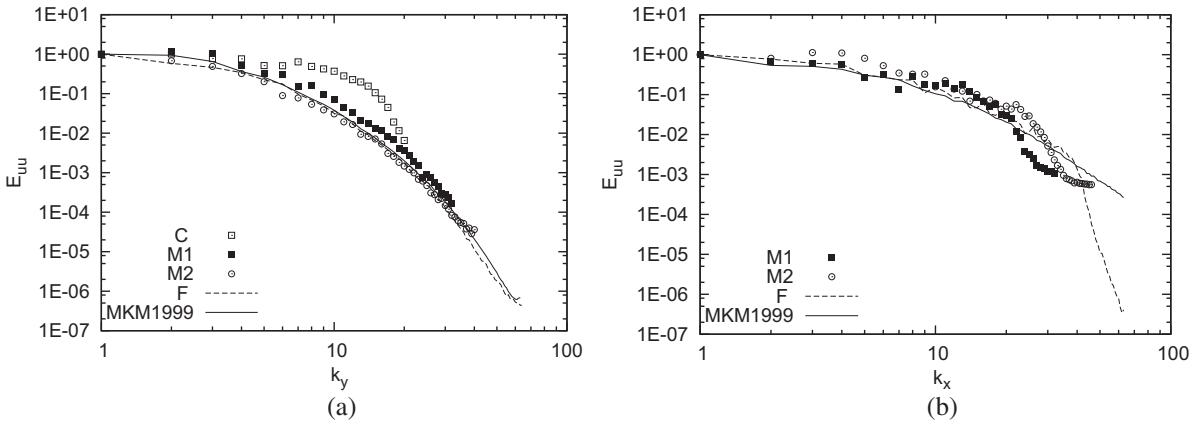

Fig. 13. One-dimensional energy spectra in spanwise (a) and streamwise (b) directions of the streamwise velocity at $z^+ = 178$.

7.4.3. Comparison with the second-order scheme

The improvement of the compact fourth-order over the second-order scheme is illustrated in Fig. 14(a). The profile of the mean streamwise velocity of the fourth-order scheme is closer to the spectral solution at the same number of grid points. The second-order scheme requires twice number of grid cells in each direction to have a result comparable with the fourth-order

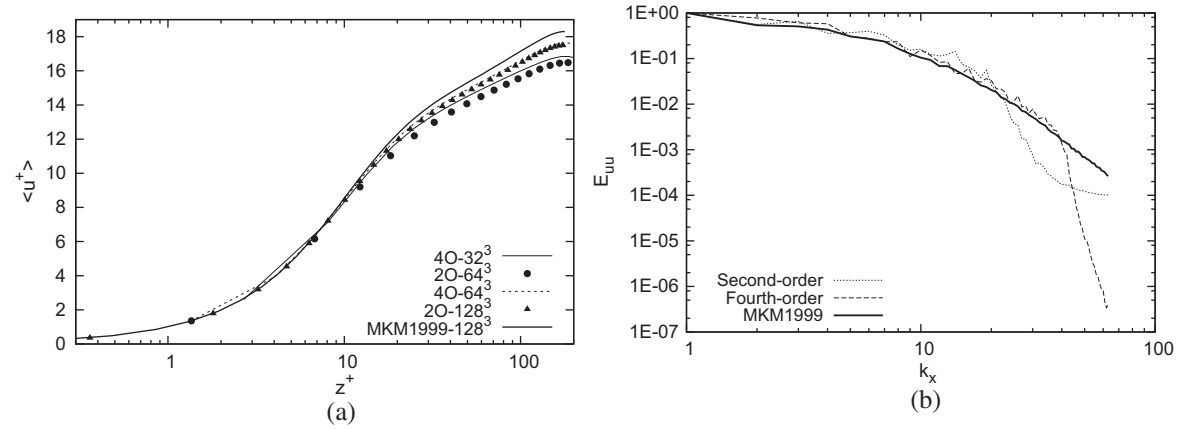

Fig. 14. Comparison of the mean streamwise velocity profiles of second-order and fourth-order scheme: (a) mean streamwise velocity, (b) one-dimensional spectra in x-direction of the streamwise velocity on grid F.

scheme. It was shown earlier that the fourth-order scheme only requires 0.7M grid cells to match the solution of spectral codes up to the second-order statistics. The second-order scheme cannot match the first-order statistics even at 2.1M i.e. three-times more cells than the fourth-order. The energy spectra E_{uu} in x-direction show an interesting result. The second-order drops sharply at $k_x \approx 25$. This means the second-order scheme can accurately capture only 40% of the whole energy spectrum while the fourth-order can capture up to 60%.

In order to provide a clear picture of the efficiency of the fourth-order scheme, we document the CPU seconds used to advance the momentum equation (Eq. (6)) per time step in Table 8. The runtimes are broken down into the computation of the momentum equation (M) and the solution of pressure (P) which includes the calculation of divergence, solution of Poisson equation and velocity correction. The computations are performed using double precision on an AMD Opteron 8216. The compiler is Intel FORTRAN and the optimization is set to *-O3*. Due to the logarithmic complexity of the FFT, the CPU-time of the solution of pressure increases fastest. It occupies 50% of the total time on the finest grid in the fourth-order scheme. At the same number of grid cells, the fourth-order is 2.4-times more expensive in average. If one considers that the fourth-order scheme requires only half of the grid cells in each direction, this means the compact fourth-order scheme can deliver a result 5-times faster than the second-order scheme *per time integration*. A larger grid size allows a larger time step, therefore the compact fourth-order scheme can be effectively 10-times more efficient than the second-order scheme. This luxury efficiency can be spent to get a more accurate solution in a shorter time.

7.4.4. Effects of second-order solution of pressure and nonlinear correction

In what follows the effects of the second-order approximation of the pressure and the nonlinear correction for convective term are investigated. The first effect is studied by keeping the approximation of the momentum and the diffusive terms at fourth-order but compute the pressure gradient and the divergence by second-order approximations. The second effect is investigated by using the fourth-order scheme but turn off the nonlinear correction.

Numerical simulations are performed again on grid C, $M1$ and $M2$. Only the mean streamwise velocity profiles on grid C are plotted in Fig. 15 which shows that the effects of the pressure treatments are very strong while those of the nonlinear correction are much smaller. Similar observations can be made on other grids as well (not shown). The fourth-order solution of pressure is therefore essential to obtain accurate solutions and a convergent scheme. The nonlinear correction takes care of the small variations on the surfaces of the momentum cells. It will not improve the accuracy of the convective term on coarse grids when the error in the approximations of momentum and convective velocities are relatively large. This effect is similar to the relationship between the truncation errors and the subgrid-scale model mentioned by Ghosal [1]. The nonlinear correction costs roughly 30% of the time used in the computation of the momentum equation. Thus when performing

Table 8
CPU-seconds per time step spent in momentum equation (M) and the enforcement of continuity (P) on an Opteron 8216.

Grid	Fourth-order			Second-order			Ratio
	M	P	Sum	M	P	Sum	
C-32^3	0.11	0.05	0.16	0.03	0.032	0.06	2.73
M1-64^3	1.08	0.73	1.89	0.19	0.621	0.81	2.34
M2-$96^2 \times 80$	4.22	3.55	7.77	0.58	2.343	2.92	2.66
F-128^3	9.72	9.80	19.52	1.56	8.716	10.28	1.90

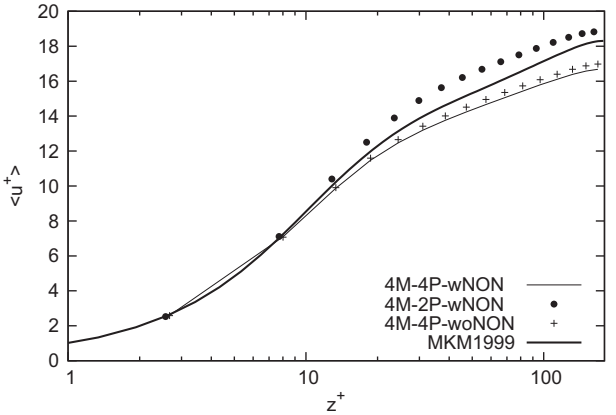

Fig. 15. Mean streamwise velocity on grid C. The thin solid line is the full fourth-order scheme (4M-4P-wNON). The circle (4M-2P-wNON) is the solution using the fourth-order scheme for convective and diffusive terms but second-order approximation of divergence and pressure gradient. The plus symbol (4M-4P-woNON) is the full fourth-order schemes without the nonlinear correction.

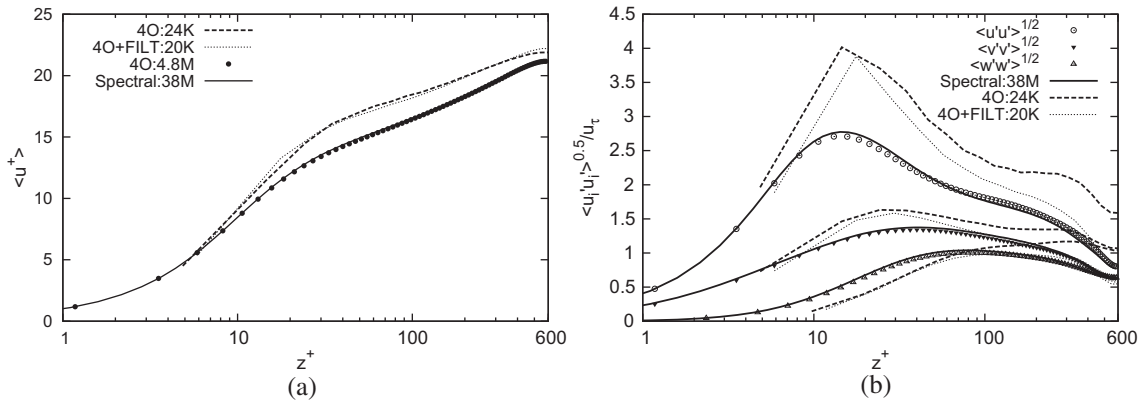

Fig. 16. Mean streamwise velocity (a) and the velocity fluctuations (b) in a turbulent channel flow ($Re_\tau = 590$) of the fourth-order scheme on 20K, 24K and 4.8M grid cells compared to spectral solution on 38 M grid points from [18].

LES and the grid spacing is much larger than the Kolmogorov length scale, the nonlinear correction can be turned off for a better cost/performance ratio. However, when performing DNS, the nonlinear correction would be necessary when highly accurate solutions (comparable to spectral codes) are sought and the grid was sufficiently fine.

7.5. Turbulent channel flow: $Re_\tau = 590$

Since the mass and momentum are fully conserved in our scheme but the discrete kinetic energy are not, the main question now is: how reliable this scheme can be when applied to high Reynolds number flow? To answer this question we perform simulations of turbulent channel flow at $Re_\tau = 590$. First we consider a relatively fine grid followed by simulations on coarser grids. In DNS, the grid resolutions have to be fine enough to capture the dynamic significant features of the flow. Sagaut [38] suggests that, for the turbulent channel flow, the grid resolution should be $[\Delta x, \Delta y, \Delta z_{min}, \Delta z_{max}]$=$[15^+, 5^+, 1^+, 10^+]$. These values are already coarser than the one surveyed in [39]. However, the previous results on M2 grid indicate that the proposed scheme could deliver the first- and second-order statistics accurately using a grid resolution significantly coarser than the suggested values. To further check if such resolutions can deliver a comparable prediction for higher Reynolds number flows, we design the fine grid here such that the respective grid resolutions are $[22.1^+, 9.2^+, 2.4^+, 13.5^+]$. This leads to $4.8M$ grid cells in total ($[N_x, N_y, N_z] = [168, 256, 144]$). Fig. 16 shows that the mean streamwise velocity profile collapses on the reference solution which was computed on 38 M grid points. The velocity fluctuations are very close to the reference solution [18] with a slightly under predicted trend. According to this result we can conclude that the fourth-order compact scheme can deliver accurate predictions for turbulent boundary layer flows with the grid resolutions 50% coarser than previously suggested. Therefore the proposed scheme is an excellent candidate for direct numerical simulation of turbulent flows.

Next, we turn our attention to the stability on coarse grids $[N_x, N_y, N_z] = 25, 25, 38]$ (24 K cells). The coarse grid here is the minimum grid resolution that can deliver a long-time stable simulation, without any kind of stabilizations or modeling. The bulk flow on this grid is over predicted by 7% and ratio of the maximum velocity to the friction velocity (U_c/u_τ) obtained with this grid is 21.7 compared to 21.3 in the reference solution. We cannot reduce the grid further because the strong transition of the gradient near the wall is a fix onset of aliasing errors. The higher the order of the scheme, the more it is affected by this error. We found that at least three cells outside the log layer and a grid stretching less than 15% are necessary for a stable simulation. We have made tests with low-pass filtering of the deconvoluted face-averaged momentum to stabilize the simulation. This filtering allows for further coarsening of the mesh to [25,25,32] cells at a slightly improved accuracy.

8. Conclusion and outlook

We have presented a fourth-order finite volume method using compact schemes for transported momentum and a divergence-free convective velocity. The accuracy of spatial approximations was studied by Fourier analysis. The deconvolution needed to approximate the momentum fluxes from the volume-averaged velocities is found to be the critical part of the whole scheme.

On staggered grids the second-order solution of pressure limits the accuracy of the solver but not as strong as observed in [12] for collocated grids. A convergence rate of third-order can be achieved on staggered grids when the pressure is only treated with second-order accuracy. This finding is supported by a comparative error analysis in Fourier space. The cell-centered deconvolution used to enforce the continuity on staggered grids has higher resolving power than the inter-cell deconvolution on collocated grids. Thus more information is preserved in the velocity field. A third-order convergence rate can be obtained whilst it is capped at second-order on collocated grids. Nevertheless, a fourth-order solution of pressure is required to reach overall fourth-order convergence.

We studied two formulations for the fourth-order convective velocities, a conservative (DF4) and non-conservative (T4). A difference between them can hardly be observed in laminar flows because of the smoothness of the field. In turbulent flows they give significantly different results on coarse grids. Therefore divergence-free formulations should be used for the convective velocity to maintain the underlying conservation properties of the Navier–Stokes equations.

The high resolution property and the efficiency of the proposed scheme were demonstrated using a turbulent channel flow in which the convergence towards the spectral solution is demonstrated. The proposed scheme was shown to deliver reasonable solutions for turbulent flows at $Re_\tau = 590$ using 24 K grid cells. On extremely coarse grid, low-pass filtering can stabilize the simulation and improve accuracy of the solution. The effective grid resolutions on $[\Delta x,\ \Delta y, \Delta z_{min}, \Delta z_{max}] \approx [22^+, 9^+, 2^+, 10^+]$ were found to be adequate for accurate predictions of turbulent channel flows with small error in third and fourth-order statistics. Increasing the grid resolutions improves these higher-order statistics. We have quantified the efficiency of the proposed scheme and found that it requires half of the resolution per coordinate direction to have a comparable result with the second-order scheme. Effectively, the fourth-order scheme can be ten-times faster than the second-order scheme in advancing the momentum per one dimensionless time unit, at a comparable accuracy. This finding is in contrast to statements of other authors who did not find crucial improvement of the performance of the higher-order schemes in turbulent channel flow.

The fourth-order solution of pressure is essential, physically and numerically. The second-order pressure will only give, at best, a third-order convergence rate for the velocities and it delivers poor solutions in turbulent channel flows. The nonlinear correction is found to be useful on a very fine grid and unimportant otherwise. It could be turned off when performing LES for a better cost/performance ratio.

For the proposed compact scheme to be a replacement of the second-order scheme in numerical simulations of turbulent flows, there are some further problems to be solved. The two most crucial problems are the parallelization of the compact scheme and the iterative solution for the projection method. Standard parallel algorithms solving tridiagonal systems on distributed memory computers require twice the number of floating point operations than the sequential algorithm. When solving the Poisson equation by iterative methods we have to deal with the 19-point Laplacian which poses a significant work load and only a few works addressing the solution of such matrices have been published to now. Therefore further research of multigrid method for these new discrete Laplacians could offer a significant improvement in the efficiency of the fourth-order compact scheme.

References

[1] S. Ghosal, An analysis of numerical errors in large-eddy simulations of turbulence, Journal of Computational Physics 125 (1996) 187.
[2] S.K. Lele, Compact finite difference schemes with spectral-like resolution, Journal of Computational Physics 103 (1992) 16.
[3] D. Gaitonde, J.S. Shang, Optimized compact-difference-based finite-volume schemes for linear wave phenomena, Journal of Computational Physics 138 (1997) 617.
[4] M.H. Kobayashi, On a class of Pade finite volume methods, Journal of Computational Physics 156 (1999) 137.
[5] J.M.C. Pereira, M.H. Kobayashi, J.C.F. Pereira, A fourth-order-accurate finite volume compact method for the incompressible Navier–Stokes solutions, Journal of Computational Physics 167 (2001) 217.
[6] M. Piller, E. Stalio, Finite-volume compact schemes on staggered grids, Journal of Computational Physics 197 (2004) 299.
[7] C. Lacor, S. Smirnova, M. Baelmansb, A finite volume formulation of compact central schemes on arbitrary structured grids, Journal of Computational Physics 198 (2004) 535.
[8] A.E. Amiri, S.K. Hannani, F. Mashayek, Evaluation of a fourth-order finite-volume compact scheme for LES with explicit filtering, Numerical Heat Transfer 48 (2005) 147.
[9] O. Shishkina, C. Wagner, A fourth order finite volume scheme for turbulent flow simulations in cylindrical domains, Computers and Fluids 36 (2007) 484.
[10] S. Nagarajan, S.K. Lele, J.H. Ferziger, A robust high-order compact method for large eddy simulation, Journal of Computational Physics 191 (2003) 392.
[11] A.O. Demuren, R.V. Wilson, M. Carpenter, Higher-order compact schemes for numerical simulation of incompressible flows. Part I: Theoretical development, Numerical Heat Transfer, Part B 39 (2001) 207.
[12] R.V. Wilson, A.O. Demuren, Higher-order compact schemes for numerical simulation of incompressible flows. Part II: Applications, Numerical Heat Transfer, Part B 39 (2001) 231.
[13] R. Knikker, Study of a staggered fourth-order compact scheme for unsteady incompressible viscous flows, International Journal for Numerical Methods in Fluids 59 (2009) 1063.
[14] S. Chakravorty, J. Mathew, A high-resolution scheme for low Mach number, International Journal for Numerical Methods in Fluids 46 (2004) 245.
[15] J. Gullbrand, An evaluation of a conservative fourth order DNS code in turbulent channel, Technical report, Center for Turbulence Research, Stanford University, 2000.
[16] Y. Morinishi, T.S. Lund, O.V. Vasilyev, P. Moin, Fully conservative higher order finite difference schemes for incompressible flow, Journal of Computational Physics 143 (1998) 90.
[17] O.V. Vasilyev, High order finite difference schemes on non-uniform meshes with good conservation properties, Journal of Computational Physics 157 (2000) 746.
[18] Moser, Kim, Mansour, Direct numerical simulation of turbulent channel flow up to $Re_\tau = 590$, Physics of Fluids 11 (1999) 943.
[19] M. Meinke, W. Schroeder, E. Krause, T. Rister, A comparison of second- and sixth-order methods for large-eddy simulations, Computers and Fluids 31 (2002) 695.
[20] J.W. Kim, D.J. Lee, Optimized compact finite difference schemes with maximum resolution, AIAA Journal 34 (1996) 887.
[21] R.W.C.P. Verstappen, A.E.P. Veldman, Symmetry-preserving discretization of turbulent flow, Journal of Computational Physics 187 (2003) 343.
[22] D.L. Brown, R. Cortez, M.L. Minion, Accurate projection methods for the incompressible Navier–Stokes equations, Journal of Computational Physics 168 (2001) 464.
[23] F.M. Denaro, On the application of the Helmholtz–Hodge decomposition in projection methods for incompressible flows with general boundary conditions, International Journal for Numerical Methods in Fluids 43 (2003) 43.
[24] A.J. Chorin, Numerical solution of the Navier–Stokes equations, Mathematics of Computation 22 (1968) 745.
[25] H.S. Stone, An efficient parallel algorithm for the solution of a tridiagonal linear system of equations, Journal of the ACM 20 (1973) 27.

[26] A. Hokpunna, M. Manhart, An approximate projection method for higher-order schemes in turbulent flows, in: 2nd GACM Colloquium on Computational Mechanics, 2007.
[27] A. Hokpunna, Compact Fourth-order Scheme for Numerical Simulations of Navier–Stokes Equations, Ph.D. Thesis, Hydromechanik, Technische Universität München, 2009.
[28] M.H. Carpenter, D. Gottlieb, S. Abarbanel, The stability of numerical boundary treatments for compact high-order finite-difference schemes, Journal of Computational Physics 108 (1993) 272.
[29] J.H. Williamson, Low-storage Runge–Kutta schemes, Journal of Computational Physics 35 (1980) 48.
[30] J.C. Hardin, J.R. Ristorcelli, C.K.W. Tam, ICASE/LaRC workshop on benchmark problems in computational aeroacoustics (CAA), in: Workshop Held in Hampton, VA, 24–26 Oct. 1994; Sponsored by NASA, Washington and Inst. for Computer Applications in Science and Engineering, 1995, pp. 24–26.
[31] D.L. Brown, Performance of under-resolved two-dimensional incompressible flow simulations, Journal of Computational Physics 122 (1995) 165.
[32] M. Malik, T. Zang, M. Hussaini, A spectral collocation method for the Navier–Stokes equation, Journal of Computational Physics 61 (1985) 64.
[33] M.M. Rai, P. Moin, Direct simulation of turbulent flow using finite-difference schemes, Journal of Computational Physics 96 (1991) 15.
[34] G. Alfonsi, G. Passoni, L. Pancaldo, D. Zampaglione, A spectral-finite difference solution of the Navier–Stokes equations in three dimensions, International Journal for Numerical Methods in Fluids 28 (1998) 129.
[35] J.M.A. Das, Direct numerical simulation of turbulent spots, Computers and Fluids 30 (2001) 533.
[36] J. Kim, P. Moin, R.D. Moser, Turbulence statistics in fully developed channel flow at low Reynolds number, Journal of Fluid Mechanics 177 (1987) 133.
[37] Z.W. Hu, Wall pressure and shear stress spectra from direct simulations of channel flow, AIAA Journal 44 (2006) 1541.
[38] P. Sagaut, Large-eddy Simulation for Acoustics, Large-eddy Simulation for Acoustics, 13th ed., 2007, pp. 89–127.
[39] P. Moin, K. Mahesh, Direct numerical simulation: a tool in turbulence research, Annual Review of Fluid Mechanics 30 (1998) 539.